Diamond nanostructures for drug delivery, bioimaging, and biosensing

Diamond nanostructures for drug delivery, bioimaging, and biosensing

Xianfeng Chen[a*] and Wenjun Zhang[b*]

[a]Institute for Bioengineering, School of Engineering, The University of Edinburgh, King's Buildings, Mayfield Road, Edinburgh EH9 3JL, United Kingdom

[b]Center of Super-Diamond and Advanced Films (COSDAF) and Department of Physics and Materials Science, City University of Hong Kong, Hong Kong SAR

[*]E-mail: xianfeng.chen@oxon.org; apwjzh@cityu.edu.hk

Abstract

Diamond features an attractive combination of outstanding mechanical, optical, thermal and electrical properties; tunable surface characteristics; and unprecedented biocompatibility. Additionally, diamond can possess unique nitrogen-vacancy emission centers that are highly photostable and extremely sensitive to magnetic fields, temperatures, ion concentrations, and spin densities. With these inherent merits, diamond in various nanoscale configurations has demonstrated a variety of distinctive applications in a broad range of fields. In particular, research on diamond nanoparticles (0-dimensional structures) and arrays of diamond nanoneedles/nanowires (1-dimensional structures) has witnessed important and exciting progress in recent years. Here, we systematically review the superior properties of diamond nanomaterials and the nitrogen-vacancy centers they contain as well as their uses in biomedical applications, including biosensing, bioimaging and drug delivery. Moreover, systematic studies of the biocompatibility and toxicity of diamond nanostructures, which constitute an important issue for the biomedical applications of diamond that has not yet been thoroughly

addressed in previous reviews, are also discussed. Finally, we present our insights into the key issues concerning these diamond nanomaterials and their future development for applications.

1. Introduction

Diamond symbolizes wealth and luxury. Although very expensive in cost, it is a valuable engineering material with important applications in high-tech electronics, optics and machining.[1-5] In particular, with the development of high-pressure, high-temperature (HPHT) and chemical vapor deposition (CVD) methods, it has become possible to artificially produce bulk diamond and 2-dimensional (2D) diamond films,[6-10] thereby substantially expanding the scope of utilization of this luxury material to a variety of ordinary commercial products. For example, diamond lenses enable optical applications under high-power radiation and in harsh environments.[11] Synthetic diamond is also highly desirable for thermal management and semiconductor packaging because of its high thermal conductivity combined with electrical isolation.[12-16] Furthermore, diamond materials have been developed for high-temperature field-effect transistors (FETs)[17] and surgical knives.[18]

Beyond bulk and 2D diamond materials, recent explorations of 1D diamond nanowires and 0D diamond nanoparticles have further broadened the applications of this material.[19-21] In this review, the term "diamond nanoparticles" is used refer to diamond crystals with diameters in a range of greater than 1 nm to approximately 100 nm, which are also called simply nanodiamonds. Fig. 1a shows atomic force microscopy (AFM) images of individual 5-nm diamond nanoparticles.[22] Fig. 1b presents a magnified image of a representative nanodiamond of 5 nm in height. Regarding 1D diamond nanostructures, this review focuses on vertically aligned nanowire, nanoneedle or nanopillar arrays and similar structures formed on flat solid substrates. Fig. 1c and d present scanning electron microscopy (SEM) images of diamond

nanoneedle arrays fabricated on silicon substrates.[19, 20, 23] Below, the fabrication of these types of diamond nanostructures is briefly described.

Diamond nanoparticles can be prepared from molecules of explosives.[21] The explosives act as a source of carbon and also provide energy for the carbon's conversion into diamond. For example, to synthesize diamond nanoparticles, an oxygen-deficient explosive mixture of 60 wt% TNT ($C_6H_2(NO_2)_3CH_3$) and 40 wt% hexogen ($C_3H_6N_6O_6$) can be detonated in a closed metallic chamber in an atmosphere of nitrogen, carbon dioxide and liquid or solid water.[21] The product comprises diamond nanoparticles of 4-5 nm in diameter and other carbon allotropes as well as impurities such as metal. To remove non-diamond carbon, the product can be treated using liquid oxidants, such as a mixture of H_2SO_4 and HNO_3. An alternative approach is to oxidize the non-diamond carbon in air or ozone-enriched air at elevated temperatures.[24, 25] Compared with liquid-phase purification, the oxidation method is more cost-effective and environmentally friendly.

Vertically aligned diamond nanostructure arrays are commonly produced via a top-down process through plasma etching.[26, 27] Typically, fabrication is performed via a two-step process consisting of the synthesis of diamond films via CVD on a substrate such as silicon followed by plasma etching to obtain the desired nanostructures, depending on the etching parameters. Because of the negative electron affinity of a hydrogen-terminated diamond surface, this plasma etching can be conveniently performed even without the assistance of a mask. The diamond films can be either polycrystalline or nanocrystalline in nature. For instance, aligned diamond nanostructures have been constructed on [001]-oriented diamond films and HPHT diamond single crystals. In these cases, the individual diamond nanostructures (e.g., nanocones and nanopillars) that are fabricated still maintain the single-crystal orientation of the starting materials.[26]

Diamond nanoparticles and vertically aligned diamond nanostructures inherit the remarkable mechanical, optical, thermal and electrical properties, the color centers, and the intrinsic biocompatibility of bulk diamond. As a result, these novel nanostructures have a great variety of applications, including chromatography, mass spectrometry, proteomics, energy storage, catalysis, electroanalysis, tribology and lubrication, tissue scaffolds, surgical implants, capacitors and batteries.[21] Moreover, nitrogen-vacancy (NV) color centers can be created in these diamond nanostructures.[28] The superior and unique characteristics of these NV centers, together with the excellent biocompatibility and surface tunability of diamond, have led to exciting advances in the biological and biomedical applications of diamond nanostructures. The progress achieved in research on diamond nanostructures has not only motivated great efforts from material scientists but also attracted broad interest from researchers in the fields of physics, chemistry, biology, and medicine.

This review focuses on the properties and applications of 0D diamond nanoparticles and arrays of vertically aligned 1D diamond nanostructures for drug delivery, bioimaging and biosensing. Because these applications are mainly enabled by the mechanical properties, surface modification capability, and biocompatibility of diamond, we first summarize the relevant studies on these properties, particularly for diamond nanostructures. Then, we introduce NV centers and their unique characteristics, which serve as the basis for the broad application of these materials in bioimaging and biosensing. In the subsequent sections, the recent progress on the utilization of two types of diamond nanostructures, namely, diamond nanoparticles and vertically aligned 1D diamond nanostructures, are surveyed with a focus on drug delivery, bioimaging and biosensing. For these applications, the biocompatibility and toxicity of these diamond nanostructures are of central importance; therefore, relevant studies on these topics are also systematically discussed. After this comprehensive overview, insights are presented regarding the future development of these two forms of diamond nanostructures.

2. Properties of diamond and diamond nanostructures

2.1. Mechanical properties

Diamond is the hardest material in the world; its excellent mechanical properties make it very useful and sometimes uniquely suitable for application when mechanical strength is required, even at the nanometer scale. As one relevant comparison, the Young's moduli of single-crystal diamond and silicon are 1141 and 162.9 GPa, respectively.[29] The Young's modulus and hardness values of diamond materials (e.g., HPHT crystals and films) vary depending on the sample preparation method used and the crystallographic orientations, and they are also affected by the measurement method and computing approach.[30] In general, a hardness of 95-131 GPa is well accepted for diamond. These superior mechanical properties make diamond an optimal choice for nano-mechanical design.[31] For diamond nanowires with a cross-sectional area of only 4.58 nm^2, at room temperature (300 K), the Young's modulus, yield strength, and fracture strength are still as high as 688, 63, and 91 GPa, respectively (Table 1).[32] The mechanical strength remains high even when the cross-sectional area decreases to only 2 nm^2 (Table 2).[32] At a diameter of greater than 3 nm, diamond nanorods are stronger than single-walled carbon nanotubes.[33]

Table 1 Mechanical properties calculated under different temperature conditions for diamond nanowires (DNWs) with cross-sectional areas of 4.58 nm^2.[32]

Temperature (K)	100	200	300	400	500
Yield strength (GPa)	74	68	63	54	53
Young's modulus (GPa)	831	753	688	633	583
Fracture strength (GPa)	122	112	91	80	68
Fracture strain	0.45	0.41	0.35	0.31	0.25

Table 2 Mechanical properties of diamond nanowires with cross-sectional areas ranging from 2 to 12.7 nm^2 at a temperature of 300 K.[32]

Cross-sectional area (nm^2)	Yield strength (GPa)	Young's modulus (GPa)	Fracture strength (GPa)	Fracture strain
2.0	29	425	45	0.19
3.2	55	635	74	0.31
4.6	63	688	82	0.33
6.2	72	764	91	0.34
8.1	75	825	98	0.31
10.3	79	834	106	0.35
12.7	80	849	111	0.31
Bulk diamond	183	1014	183	0.35

2.2. Surface modification

The surfaces of diamond nanostructures play an important role in determining the utility and biocompatibility of these nanostructures in biological and medical applications, such as targeted drug delivery, selective biosensing, and effective therapy. The first step of diamond surface modification often involves harsh treatment with strong chemicals or plasma irradiation to introduce functional groups onto the surface. Once surface functional groups have been established, various linker molecules or biomolecules, including biomarkers, therapeutic drugs, and genes, can be grafted onto the surface. A range of methods[34-42] have been reviewed by Nagl *et al.* with an illustration provided in Fig. 2.[43] A number of representative surface modification methods are briefly described as follows: 1) Oxidative treatment can create carboxyl groups, which are characteristic of the most highly oxidized state of a carbon surface, on the surface of diamond, thereby allowing further connection with alcohol or amine derivatives.[44] Such oxidation is generally performed in a mixture of strongly oxidizing acids, such as equal amounts of H_2SO_4, HNO_3, and $HClO_4$ or HCl, HNO_3, and H_2SO_4.[24, 45, 46]

Alternatively, oxidative treatment can also be performed in a mixture of sulfuric acid and hydrogen peroxide with a volume ratio of 3 to 1.[47] 2) Halogenation, such as thermal or plasma fluorination, of the surface enables diamond to react with lithium organic compounds, resulting in amino or acid terminations.[42, 48-50] 3) Oxygen-containing groups carrying C=O moieties on the surface of diamond can be reduced to –OH with borane, which permits the subsequent growth of various silanes, including assorted foundational groups such as epoxy, amino, sulfido, methacryloxy, carboxyl, and PEG groups.[34] 4) The surface of diamond can be hydrogenated at elevated temperatures or in a hydrogen plasma to produce C-H bonds.[51] 5) The thiolation of diamond nanoparticles can also be performed.[52] Such thiolation is achieved via a two-step process. First, detonation diamond nanoparticles are treated with $LiAlH_4$ to reduce the surface carboxyl and carbonyl groups and to generate hydroxyl groups. Second, the hydroxyl groups are converted into thiol groups by means of treatment with hydrobromic acid and acetic acid. Additional methods for the surface modification of diamond can be found in the reviews by Krueger *et al.*[46, 53, 54] and Mochalin *et al.*[21] As can be seen from this summary, the surface of diamond can be flexibly tuned depending on the facilities available and the needs of the application.

2.3. Biocompatibility of diamond

Diamond is chemically inert and does not release toxic chemicals even in harsh environments; thus, these properties endow diamond nanostructures with intrinsic biocompatibility. This represents a considerable advantage of diamond nanostructures compared with II-VI semiconductor quantum dots, which often contain toxic heavy metals; consequently, their oxidation leads to slow liberation of heavy metal ions, correspondingly giving rise to high toxicity.[55-57] Extensive studies have been conducted to explore the *in vitro* and *in vivo* toxicity of diamond nanostructures.[58-61] Overall, the results suggest that diamond

nanostructures exhibit extremely high biocompatibility. The details will be discussed in a later section.

3. Nitrogen-vacancy centers in diamond

Methods of biological labeling and sensing have received significant interest because of their applications in not only basic cell biology research but also cancer diagnosis and imaging. Extensive efforts have been devoted to this field, and a variety of nanomaterials have been developed for this purpose.[62-70] For instance, II-VI semiconductor quantum dots have been extensively studied for bioimaging and sensing applications.[64, 71] However, this group of materials generally suffers from the problems of photobleaching, photoblinking, and particularly cytotoxicity, which severely limit their use to mostly *in vitro* work and narrow their scope of application.[72] To overcome these limitations, silicon nanocrystals and carbon dots, which feature higher photostability and better biocompatibility, have been developed.[73-80] Although silicon nanocrystals and carbon dots have demonstrated increasing importance in the field of biological labeling and sensing, important questions still remain regarding a complete understanding of their fluorescence mechanism and rational control of their emission characteristics. Unlike these materials, the biological labeling and sensing behavior of diamond nanoparticles is known to rely mainly on the formation of well-established fluorescent NV centers. Together with the facile surface modification and excellent photostability and biocompatibility of diamond nanoparticles, the high sensitivity of NV centers endows these nanoparticles with unprecedented performance in bioimaging and biosensing. In this section, the general nature, methods of production, and characteristics of NV centers are summarized.

3.1. The nature of nitrogen-vacancy centers

NV centers are a type of point defect in diamond. As shown in Fig. 3a, an NV center is composed of a substitutional nitrogen atom (blue ball) and a bounded lattice vacancy (white

ball).[28] NV centers in diamond are luminescent color centers. A high concentration of NV centers lends a pink color to a diamond crystal.

A single NV center may carry a negative charge or may possess a neutral charge state, denoted by NV^- and NV^0, respectively. When excited by green light (532 nm), such a color center emits in the near-infrared region. The fluorescence spectrum of a single NV center exhibits zero-phonon lines (ZPLs) that are characteristic of NV^0 and NV^- (Fig. 3b).[28]

In the neutral charge state, an NV defect has one unpaired electron. In the negative charge state, an NV defect has two unpaired electrons, which form an integer spin (S=1), and the defect has associated electron energy levels of triplet ground (^3A) and excited (^3E) states (here, the number 3 indicates that 3 m_s spin states of -1, 0, and 1 are allowed). In the absence of an external magnetic field, the ground-state spin sublevels corresponding to $m_s=\pm1$ are degenerate and separated from $m_s=0$ (the $m_s=\pm1$ levels have similar energies). Upon excitation with light (green arrow), electrons are excited from the ^3A state to the ^3E state. Subsequently, the electrons return from the ^3E state to the ^3A state and release energy by emitting light (red arrows). During these processes, the transitions between the ground and excited states conserve the spin state of $m_s=0$ or ±1. On occasion, the excited state (^3E) may transition into a metastable singlet state (^1A), from which the electrons will return to the ground state through non-radiative emission (black arrows). The excited states corresponding to $m_s=\pm1$ have a higher probability of inter-system crossing.

In the presence of a resonant magnetic field, the $m_s=\pm1$ energy levels shift in opposite directions (the difference between these two energy levels increases), and the electron spin undergoes a transition from $m_s=0$ to $m_s=\pm1$ in the ground state (Fig. 3c).[28] This leads to more inter-system crossing and, correspondingly, to a dramatic decrease in fluorescence emission intensity. From the description given above, it can be seen that the spin state of the electrons in

an NV center can be conveniently determined based on fluorescence variations, namely, through optically detected magnetic resonance (ODMR). Fig. 3d shows the ODMR spectra of a single NV spin under different magnetic fields.[28] It is clear that an external magnetic field causes the energy levels of the NV electron spin states to split. An important feature of ODMR is that it can be detected at the single-spin level under ambient conditions, such as room temperature.

As described above, the electron spin states of NV centers are very sensitive to magnetic fields. This phenomenon can be conveniently exploited for sensing subtle changes. Fig. 4a shows the setup for a magnetic field imaging experiment.[81] In this setup, a diamond nanocrystal containing a single NV center is attached to the tip of an AFM cantilever, which is used to profile the magnetic field generated by a small magnetic structure at the nanometer scale. Fig. 4b presents an optical image of a diamond nanocrystal mounted on an AFM tip. Fig. 4c presents an AFM image of the magnetic nanostructure at the top and a corresponding magneto-optical image of the same magnetic structure at the bottom. In this demonstrative work, a single NV center was employed as an atomic-scale magnetic field sensor. The spatial resolution associated with the size of diamond nanoparticles can be as small as a few nanometers or even at the sub-nanometer level, thus offering a sufficiently high sensitivity to probe single electron spins.[82, 83]

In addition to magnetic fields, the spin states of NV centers, particularly NV^- centers, are also sensitive to interfering factors such as temperature, ion concentration, electric fields, and crystal stress. Because of these unique properties, the fluorescence signals from NV^- centers can be used as a sensitive probe in a variety of applications.

3.2. Production of nitrogen-vacancy centers

In diamond nanoparticles with a negligible concentration of nitrogen, NV centers can be created via N^+ ion implantation followed by annealing at high temperatures.[84] By contrast, if a

diamond material already contains nitrogen impurities, then NV centers can be generated via particle irradiation followed by annealing. Various types of high-energy particles have been used for this purpose, such as electrons, protons, ions, and neutrons. An example of a procedure for producing NV centers via proton irradiation is as follows:[85] 1) synthetic type Ib (typical nitrogen concentration of 100 ppm) diamond powders of approximately 100 nm in size are processed in strong oxidative acids; 2) a diamond powder film is prepared by depositing the purified diamond suspension on a silicon wafer, followed by drying; and 3) the diamond powder film is irradiated with a 3-MeV proton beam at a dose of 5×10^{15} ions/cm^2 and then subjected to annealing at 800 °C in vacuum. It is understood that irradiation creates vacancies in a diamond lattice, whereas high-temperature annealing drives the migration of the vacancies to nitrogen impurities, thereby leading to the development of NV color centers. This method produces a concentration of NV centers of approximately 1×10^7 centers/μm^3, which is equivalent to approximately 1×10^4 centers per 100-nm diamond nanoparticle. Upon excitation with green light, the emission of the diamond nanoparticles spans wavelengths from 600 to 800 nm. Compared with nanodiamonds produced using the same procedure but without exposure to proton irradiation, irradiated diamond nanoparticles possess a fluorescence intensity that is 100 times stronger.[85]

Despite the success achieved using such procedures, high-energy irradiation and vacuum annealing at elevated temperatures require sophisticated and costly facilities. To address this problem, Chang *et al.* reported a method of mass-producing diamond nanoparticles with high fluorescence.[86] In this approach, the nanodiamonds are synthesized through ion bombardment (irradiation) of synthetic type Ib diamond powders using 40-keV He^+ ions at a dose of approximately $1x10^{13}$ ions/cm^2. He^+ ions have a very high damaging efficacy; a 40-keV He^+ ion is able to produce 40 vacancies in diamond, whereas a 2-MeV e^- or a 3-MeV H^+ ion can generate only 0.1 or 13 vacancies, respectively.[87, 88] Thus, the stronger damaging capability of

40-keV He^+ bombardment can considerably reduce the required ion dose and facilitate the large-scale production of NV centers in diamond nanoparticles.

To further reduce the cost of NV center production, Baranov *et al.* reported an alternative approach for generating a high concentration of fluorescent NV^- centers through the HPHT sintering of diamond nanoparticles of approximately 4-5 nm in size.[89] In this method, commercial diamond nanoparticles are first purified in highly concentrated hydrochloric acid (HCl) with the aid of ultrasonication. Then, the nanoparticle suspension is repeatedly treated with 38% HCl, followed by washing in boiling distilled water. Finally, the diamond powder is sintered in an HPHT system at 800 °C under a pressure of 6 GPa for 11 s. This method enables the production of a very high concentration of NV^- centers, i.e., up to one NV^- center per nm^3.

3.3. Characteristics of nitrogen-vacancy centers

To track and image a single molecule or particle within a cell using fluorescent probes, it is usually necessary to avoid interference from the fluorescence of various ubiquitous endogenous components, including collagens, porphyrins, and flavins. Typically, these molecules absorb light at wavelengths ranging from 300 to 500 nm and emit at wavelengths between 400 and 550 nm. Diamond nanoparticles exhibit emission ranging mainly from 550 to 800 nm under excitation with green light, making diamond nanoparticles a desirable probe for bioimaging (Fig. 3a).[28, 85, 86, 90-92] Within this wavelength range, to get a strong signal in imaging, it is still required that the fluorescence probe should possess strong absorption and emission. In line with this, NV^- centers in diamond nanoparticles exhibit strong absorption at approximately 560 nm and emission at approximately 700 nm. The absorption cross section of such an NV^- center at the band center has been reported to be approximately 5×10^{-17} cm^2, which is comparable to that of dye molecules.[85, 93] One recent study has shown that the absorption cross section of an NV center at a wavelength of 532 nm is $(0.95\pm0.25)\times10^{-16}$ cm^2.[94] It has been

demonstrated that a single 11-nm diamond nanoparticle containing 3 NV^- centers possesses dramatically stronger photoluminescence than does a single molecule of the red fluorescent protein DsRed-Monomer.[95] Moreover, fluorescence lifetime measurements indicate that the fluorescence decay of diamond nanoparticles has a fast component of 1.7 ns (4%) and a slow component of 17 ns (96%), as shown in Fig. 5a.[90] The latter value is much longer than those for Alexa Fluor 546 (approximately 4 ns) and cell and tissue autofluorescence (approximately 3 ns), which is particularly beneficial for isolating the emission of diamond nanoparticles from the background signals with the assistance of time-gating approaches.[96-98]

Photostability is another important factor to be considered with regard to fluorescent probes used in biosensing applications. Yu *et al.* demonstrated that fluorescent nanodiamonds possess much better photostability than do polystyrene nanospheres.[79] In this experiment, no sign of photobleaching was observed in the nanodiamonds even after 8 hours of continuous illumination under an Hg lamp. In stark contrast, under the same excitation conditions, the fluorescence of 0.1-μm red fluorescent polystyrene nanospheres decreased to nearly zero after only 0.5 h of illumination.[85] Similarly, Fu *et al.* studied the fluorescence properties of individual diamond nanoparticles using Alexa Fluor 546 as a reference.[90] The results indicated that both 100- and 35-nm diamond nanoparticles possess excellent photostability over a period of 300 seconds under 532-nm excitation at a power density of 8×10^3 W/cm^2, whereas single molecules of Alexa Fluor 546 suffer bleaching of their fluorescence within only 12 seconds (Fig. 5b).

Gruber *et al.* have also shown that the fluorescence of NV centers is highly stable even under excitation at an extremely high power of 5 MW/cm^2.[99] In contrast to the outstanding photostability of nanodiamonds, the photobleaching of quantum dots has been widely reported. For instance, under exposure to an Ar-Kr continuous wave (CW) laser operating at 468 nm and 20 kW/cm^2, core/shell CdSe/ZnS quantum dots have been found to experience photobleaching

after approximately 2-3 min in air and 10-15 min in nitrogen.[100, 101] Moreover, the photobleaching of carbon dots has also been observed even under much weaker illumination.[102] The observed excellent photostability of nanodiamonds is considered to be due to the localization of the excited state of each color center around the corresponding impurity atom, whereas in a quantum dot, the excited state is delocalized over its entire volume. In addition, the energy levels of the color centers in diamond are well separated from the valence and conduction bands of the material, which leads to the trapping of photoelectrons within these energy levels, even under high-power laser illumination.[103]

In addition to the above good characteristics to achieve high quality imaging, diamond nanoparticles also possess the following advantages that are very useful for quantitative analysis. Firstly, unlike that of other fluorescent nanomaterials such as semiconductor quantum dots, silicon nanocrystals and carbon dots, the fluorescence of diamond nanoparticles is not sensitive to surface modification and functionalization. The reason for this insensitivity is that the fluorescence of a diamond nanostructure originates from point defects within the interior of the structure.[85, 90] As shown in Fig. 6a, under irradiation with 3-MeV H^+ ions and 40-keV He^+ ions, the fluorescence intensities are different because of the different concentrations of NV centers generated by the irradiation, but the emission spectra have nearly the same profile. Fig. 6b further demonstrates that the fluorescence intensities of diamond nanoparticles of three different sizes show a similar linear dependence on the excitation laser power.[86] These observations suggest that the fluorescence intensities of diamond nanoparticles depend on their bulk properties, with negligible influence from the particles' surface characteristics. By contrast, the fluorescence properties of semiconductor quantum dots, silicon nanocrystals and carbon dots, including their emission peaks and intensities, are dramatically influenced by surface modification and their working environments,[104-107] and this sensitivity can cause serious problems in the interpretation of spectroscopic results and quantitative analysis. It is

worth nothing here that the emission spectrum profile can still be easily tuned by conjugating with fluorescent dyes[108] or semiconductor quantum dots[109] if needed to lend their flexibility in applications.

Secondly, it has also been observed that diamond nanoparticles do not exhibit fluorescence blinking at a time resolution of 1 ms.[90] Because photoblinking may cause fluctuations in fluorescence intensity and thus cause difficulties in quantitative analysis, the non-blinking behavior of diamond nanoparticles is another aspect in which diamond nanoparticles are superior to semiconductor quantum dots and silicon nanocrystals, which both exhibit photoblinking.[110-113]

4. Diamond nanoparticles for bioimaging, biosensing and drug delivery

4.1. Fluorescence imaging

Diamond nanoparticles have been widely employed for fluorescence imaging in various applications because of their collectively outstanding properties. Fig. 7a shows an overlay of bright-field and fluorescence images of a HeLa cell after the internalization of fluorescent nanodiamonds. The image indicates that the diamond nanoparticles are predominantly located in the cytoplasm of the cell after intracellular uptake. In the corresponding fluorescence image presented in Fig. 7b, two individual diamond nanoparticles separated by 1 μm can be identified.[90] Because of their high brightness and photostability, the motion of individual diamond nanoparticles can be tracked over long durations. For example, Fu *et al.* tracked a diamond nanoparticle for 13.9 s and found that the particle experienced Brownian motion confined with a 1×1 μm^2 area.[90] In another study by the same group, Chang *et al.* monitored the movement of an individual nanodiamond within a live HeLa cell for more than 200 s (Fig. 7c).[86] Through a mean square displacement analysis of the 3D trajectories, the diffusion coefficient of nanoparticles internalized in living cells can be determined.[86, 114] Collectively,

these experiments demonstrate that fluorescent diamond nanoparticles can be a desirable probe for *in vivo* imaging and long-term tracking as cellular biomarkers. The work illustrated in Fig. 7c also indicates that the imaging can be realized with high temporal and spatial resolution. To prove this, Epperla *et al.* employed diamond nanoparticles as fluorescent trackers to monitor the intracellular transport of proteins through tunneling membrane nanotubes.[115] Bovine serum albumin (BSA) and green fluorescent protein (GFP) were coated on diamond nanoparticles of approximately 100 nm in diameter by means of physical adsorption. The motion of the protein-decorated diamond nanoparticles through the tunneling nanotubes could be continuously monitored for longer than 10 min. Furthermore, Liu *et al.* recently demonstrated the use of protein-conjugated fluorescent diamond nanoparticles as imaging probes. In that work, the diamond nanoparticles were modified with transforming growth factor (TGF). Such nanoparticles can specifically bind to TGF-beta receptors, which play an important role in immune suppression and the metastasis of cancer cells. An understanding of TGF-beta receptors and their pathways is very important for the development of cancer therapies. Therefore, the authors used TGF-coated diamond nanoparticles to study the trafficking process of TGF-beta receptors. This strategy offered localization accuracies of 8 nm in the *xy* directions and 16 nm in the *z* direction, which are better than those of conventional organic dyes for 3D imaging.[116] These two examples validate a powerful tool of using fluorescent nanodiamonds for long-term imaging of the intracellular delivery of proteins. The understanding of the proteins' transmembrane pathways and mechanisms will greatly contribute to the development of better therapeutic medicines to treat diseases.

With their superior photostability and improved localization accuracy, diamond nanoparticles can also be applied for super-resolution microscopy using the stimulated emission depletion (STED) technique.[117, 118] Through this method, multiple NV^- centers in individual diamond nanoparticles can be resolved, and a remarkable resolution of

approximately 6-10 nm is achievable (Fig. 7d and e).[117, 119, 120] With such an ultra-high resolution, the applications of using fluorescent diamond nanoparticles in cell biology are expected to be tremendously extended.

The low exocytosis of fluorescent diamond nanoparticles from cells is another beneficial factor enabling their long-term imaging. The extent of exocytosis of fluorescent diamond nanoparticles from human cancer cell lines has been determined to be only approximately 15% or less after 6 days of labeling in 489-2.1 multipotent stromal cells and HeLa cells.[60] By virtue of this low exocytosis combined with the advantages of chemical and photophysical stability, diamond nanoparticles have been used to track AS-B145-1R breast cancer cells, which is used as a model cell line for quiescent cancer stem cells (CSCs), for longer than 20 days.[121] For comparison, when D-penicillamine-coated CdSe/ZnS core/shell quantum dots (8 nm in diameter) were tested in live HeLa cells, a significant fraction of the endocytosed quantum dots were exocytosed with a half-life of only 21 min; approximately 50% of the quantum dots were exocytosed after 100 min after the nanoparticle incubation solution was replaced with cell medium.[122] It has also been observed that for silicon quantum dots in human umbilical endothelial cells (HUVECs), approximately 60% are removed from cells after 250 min.[123] Moreover, the exocytosis half-life of carbon dots in rat adrenal pheochromocytoma cells and rat Schwann cells has been revealed to be approximately 2 hours, with more than 70% of the carbon dots having been exocytosed after 1 day.[124]

4.2. Magnetic resonance imaging

Magnetic resonance imaging (MRI) is capable of achieving non-invasive 3D elementally selective mapping without radiation and is consequently a widely used technique in medicine and neuroscience. However, the spatial resolution of conventional MRI is limited to tens of micrometers or even millimeters. Recently, diamond nanoparticles with NV centers have been

employed for MRI.[82, 83, 125-131] Because of the high sensitivity of the electron spin states of NV centers to magnetic fields, a considerable improvement in the resolution of MRI has thus been demonstrated, bringing this resolution to the nanometer level.

Grinolds *et al.* developed the first 3D spatial mapping technique for dark electronic spins on and near a diamond surface, in which lateral and vertical resolutions of 0.8 and 1.5 nm, respectively, were demonstrated.[83] In addition to electron spins, NV^- centers have also been employed to sense nuclear spins, which have magnetic moments that are at least 600 times smaller than those of electron spins. Rugar *et al.* utilized NV centers to detect the oscillating magnetic field generated by protons and demonstrated a spatial resolution of 12 nm for the 2D ^{1}H NMR imaging of a poly(methyl methacrylate) (PMMA) sample using a single NV center in diamond.[82] Similarly, using a single NV center embedded at approximately 7 nanometers below the surface of a bulk diamond, Staudacher *et al.* detected ^{1}H nuclear spins from single $(5\text{-nm})^3$ voxels of various fluid and solid organic samples under ambient conditions.[132] In addition to detecting ^{1}H nuclear spins, Devience *et al.* showed that NV centers in diamond can be used in NMR spectroscopy and MRI for detecting various nuclear species, including ^{1}H, ^{19}F, and ^{31}P, in non-uniform samples (with varying concentrations of nuclear spins) under ambient conditions.[126] Zhao *et al.* and Müller *et al.* further demonstrated that NV centers can be applied to achieve single-nucleus sensitivity to ^{13}C and ^{29}Si spins.[127, 133] With these demonstrated ultra-high resolution of NV-center-based MRI, we not only extend its application to the study of the structures of samples at the molecular level but also enhances its practical applicability in the life sciences and healthcare. McGuinness *et al.* pioneered the tracking of individual fluorescent nanodiamond NV centers within living HeLa cells by detecting their magnetic resonance. In this manner, the locations, orientations, spin levels and spin coherence times of NV centers can be measured with nanoscale precision.[134] NV centers have also been employed for the imaging of bioprocesses and the sensing of biomolecules.[28, 128, 135-138] For instance, by using diamond

nanoparticles with NV centers, the operation of cell membrane ion channels can be monitored with a temporal resolution of 1-10 milliseconds and a spatial resolution of nanometers.[139] Very attractively, this method enables single-protein detection.[140] By virtue of its inherent advantages, it is expected that NV-center-based MRI technology can be applied to probe intracellular electrons and, potentially, nuclear spins in single biological molecules (Fig. 8).[28]

4.3. Sensing based on optically detected magnetic resonance

As described in Section 3.1, ODMR allows diamond nanoparticles with NV centers to respond in an ultrasensitive way to external interfering parameters that can affect the spin states of NV^- centers. One potential application of this technique is to measure environmental temperature changes using nanodiamonds as quantum thermometers. It is always challenging to probe temperature variations within a local volume at the nanometer scale, particularly in living systems. Kucsko *et al.* demonstrated the ability to monitor local temperature variations in a living human embryonic fibroblast using nanodiamonds as probes.[141] The experimental design is illustrated in Fig. 9a-b. In this experiment, nanodiamonds and gold nanoparticles were introduced into the cell. The gold nanoparticles absorbed the energy of laser illumination, thereby enabling control of the local temperature, and precise spectra of the NV spins in the nanodiamonds were collected to realize temperature mapping at the subcellular level. Because the value of the transition frequency (Δ) between the $|m_s = 0\rangle$ and $|m_s = \pm1\rangle$ states is directly related to the temperature ($d\Delta/dT=-2\pi\times77$ kHz/K) because of thermally induced lattice strains, a temperature measurement precision as small as 1.8 mK and a spatial resolution as small as 200 nm were demonstrated in this experiment. Compared with other reported approaches, as illustrated in Fig. 9c, it is obvious that spectroscopy based on NV centers in nanodiamonds by means of ODMR offers an excellent combination of temperature accuracy (1.8±0.3 mK) and spatial resolution (approximately 100 nm). Recently, Tzeng *et al.* also applied this technique to achieve the real-time monitoring of temperature variations of over ±100 K.[142]

4.4. Drug and gene delivery using diamond nanoparticles

4.4.1. Diamond nanoparticles in drug delivery

Many modern drugs that are therapeutically important suffer from poor water solubility, which limits their clinical applications. Various approaches have been explored to solve this problem, such as utilizing block-copolymer-stabilized nanoemulsions, polymeric micelles, or self-aggregated nanoparticles or loading in liposomes.[143-148] As an alternative approach, diamond nanoparticles have also been complexed with poorly water-soluble drugs to enhance their dispersion in water while maintaining drug activity.[149] For instance, Chen *et al.* showed that diamond nanoparticles (4-6 nm in diameter) functionalized with carboxyl groups can adsorb drug molecules through physisorption and electrostatic interactions, thereby facilitating the dispersion of these molecules in an aqueous solution. The surfaces of diamond nanoparticles have been demonstrated to play a key role in how they interface with drug molecules. This approach has been applied to enhance the dispersibility in water of various drugs with poor water solubility, including purvalanol A for liver cancer treatment, 4-hydroxytamoxifen for breast cancer therapy, and dexamethasone for anti-inflammation.[58]

In addition to *in vitro* demonstrations, diamond nanoparticles have also been employed to deliver various water-insoluble drugs, e.g., sorafenib, for *in vivo* cancer therapy.[150] Sorafenib is a potential medicine for the treatment of metastatic gastric cancer. However, it demonstrates very poor solubility in water and even in buffered solutions with pH values ranging from 1.2 to 7.4, resulting in extremely low oral bioavailability. To improve the drug's dispersion in water, sorafenib was mixed with diamond nanoparticles to form diamond-sorafenib clusters. Then, these clusters were coated with an amphiphilic lipid, distearoylphosphatidylethanolamine-poly(ethylene glycol) (DSPE-PEG), as illustrated in Fig. 10a. The efficacy of the lipid-coated nanodiamonds loaded with sorafenib (SNDs) was evaluated using tumor xenograft mice as the

animal model. The group treated with SNDs displayed significant inhibition of tumor growth compared with others treated with an equivalent dose of sorafenib, as presented in Fig. 10b-d. In addition, the mice treated with SNDs also showed a dramatic reduction in the number of metastatic nodules in the liver and kidneys (Fig. 10e and f).[150] The metastasis accounts for over 90% of cancer-associated death and is one major challenge in cancer therapy, so the development of such technology is highly desirable.

In addition to facilitating the delivery of water-insoluble drugs, nanodiamonds can also be used to enhance drug efficacy. In a study by Chow *et al.*, diamond nanoparticles were used to aid in the delivery of an anticancer drug, DOX, for treatment in models of drug-resistant breast cancer (4T1) and liver cancer (LT2-M). It was found that the tumors expelled the nanodiamond-DOX complexes to a lesser extent than they did free DOX molecules, and the blood circulation time of the complexes was 10 times longer than that of free DOX molecules. The former will allow DOX to be more effective in tumor treatment and the latter increase DOX delivery to the tumor. Moreover, the use of nanodiamond-DOX complexes dramatically alleviated the problems of severe toxicity and myelosuppression that were observed for the free DOX molecules. As a result, the nanodiamond-DOX complexes could efficiently shrink the size of the tumors.[151] It has also been demonstrated that nanodiamonds can improve DOX accumulation in lung tissue and thus inhibit lung metastasis in breast cancer.[59] With convection-enhanced delivery, a local infusion technique for the direct delivery of drugs to the central nervous system, nanodiamond-DOX complexes have been demonstrated to serve as a powerful treatment against brain tumors.[152]

Besides DOX, many other drugs have been delivered with the assistance of diamond nanoparticles. For example, nanodiamonds loaded with daunorubicin (DNR) can overcome multidrug chemoresistance in leukemia,[153] and epirubicin-adsorbed diamond nanoparticles can effectively kill both normal cancer cells and cancer stem cells, resulting in potent inhibition of

secondary tumor growth.[154] Moreover, Cui *et al.* used diamond nanoparticles to deliver cisplatin[155] and found that sodium-alginate-functionalized diamond nanoparticles could increase drug accumulation and retention time in tumor cells.

In addition to single-drug therapies, diamond nanoparticles can also be used to deliver a combination of several drugs in a single treatment for a synergistic effect. For instance, Wang *et al.* demonstrated that an optimal combination of nanodiamond-DOX, nanodiamond-mitoxantrone, nanodiamond-bleomycin, and free paclitaxel resulted in the best therapeutic efficacy against multiple breast cancer cell lines among a variety of combinations of free drug molecules and nanodiamond-drug molecules.[156]

As an alternative to using diamond nanoparticles as carriers for direct drug delivery, it has recently been demonstrated that properly surface-modified diamond nanoparticles can be used to induce vascular barrier leakiness to indirectly facilitate drug delivery.[157] In these experiments, a monolayer of endothelial cells was cultured to mimic the vascular barrier in blood vessels. Upon treatment with nanodiamonds as illustrated in Fig. 11a, the vascular barrier became leaky (Fig. 11b), which allowed an increased amount of DOX to penetrate the vascular barrier and consequently led to increased cell death (Fig. 11c and d). The results indicate that $–NH_2$-modified diamond nanoparticles demonstrate a higher potency in inducing vascular leakage compared with bare nanodiamonds or nanodiamonds terminated with –COOH. The leakiness was found to be caused by the increased generation of reactive oxygen species (ROS) upon treatment with diamond nanoparticles. It remains unknown whether other types of nanostructures can also cause leakiness of vascular barriers, although such a result could be expected because it is common for the application of nanomaterials to induce ROS production.[158, 159] Tumors at earlier stages are more responsive to treatment. However, the blood vasculature around early-stage tumors is not leaky. Therefore, the ability of diamond

nanoparticles with proper surface termination to induce vascular barrier leakiness offers a new pathway for the early therapy of cancers.

The drug delivery work described above makes use of various characteristics of diamond nanoparticles, such as their suitable size, high aqueous dispersibility, and ease of surface modification. In addition to these characteristics, the outstanding mechanical properties of diamond also give rise to several other interesting and unique applications of nanodiamonds in clinical medicine. Recently, Lee *et al.* applied diamond nanoparticles to form a composite with gutta-percha for root canal therapy (RCT).[160] Gutta-percha is a conventional filler material used to fill the root canal space, but it suffers from several limitations, such as a tendency to induce root canal reinfection and poor mechanical properties. In the reported approach, the diamond nanoparticles were functionalized with amoxicillin to prevent infection. The diamond material was chosen to improve the mechanical properties of the filler material. Moreover, Ryu *et al.* have also developed alendronate-conjugated diamond nanoparticles to achieve bone-targeted delivery for osteoporosis treatment.[161]

4.4.2. Diamond nanoparticles in gene transfection

Gene therapy provides the opportunity to treat certain diseases that are otherwise difficult to cure. In gene therapy, DNA and siRNA must be delivered to the cytoplasm or nuclei of cells to be functional. Thus far, a variety of methods have been developed for gene delivery, including methods using various nanomaterials.[162-165] Diamond nanoparticles have also found a role in gene transfection because of their superior properties. Martin *et al.* treated nanodiamonds obtained via detonation with $FeSO_4$ and H_2O_2 under strong acidic conditions. Through this process, the size of the nanoparticles was reduced from 7.20 to 4.77 nm, and their surfaces were populated with hydroxyl groups. Subsequently, these nanoparticles were modified with triethylammonium and electrostatically paired with negatively charged GFP

plasmid DNA for successful gene expression.[166] Zhang *et al.* used polyethyleneimine (PEI800) to modify diamond nanoparticles and then applied them for DNA delivery (Fig. 12a). This led to a 70-fold increase in transfection compared with PEI800 alone, while the cytotoxicity remained very low.[167] With this approach, transfection efficiency comparable to that of PEI25K can be achieved but with significantly lower cytotoxicity (Fig. 12b and c). This method can also be applied for siRNA delivery, and siRNA transferred by diamond nanoparticles (approximately 7 nm in diameter) has been found to efficiently inhibit the gene expression of EWS/FLI-1 in a Ewing sarcoma cell line.[168] The silencing of this gene has been found to improve the cytotoxic effect of the anticancer drug vincristine.[169, 170] Recently, diamond nanoparticles were also shown to be able to deliver cytosine-phosphate-guanine (CpG) oligonucleotides (ODNs) for efficient cancer immunotherapy.[171] It was found that diamond nanoparticles could increase the cellular uptake of CpG ODNs by approximately three orders of magnitude. This nanosystem induced long-term immunoregulatory activity that could last for 3 days at the cellular level and 2 days in a mouse model. When the nanostructures were tested in two murine tumor models, including B16 melanoma and 4T1 breast carcinoma xenografts, tumor growth was substantially inhibited.

When nanomaterials (e.g., nanoparticles) are employed for drug and gene delivery, complexes consisting of the drug/gene and the nanomaterial enter cells through endocytosis and are then confined in endosomes or lysosomes. Consequently, the escape of the confined complexes into the cytoplasm of the cells is essential for them to be effective, but this is often a problem for many nanomaterials. To address this issue, Chu *et al.* fabricated diamond nanoparticles with sharp features and demonstrated that these nanodiamonds could easily enter cells via micropinocytosis.[172] Advantageously, shortly after intracellular uptake, these nanodiamonds are capable of rupturing the endosome membrane and escaping into the

cytoplasm. This feature makes such nanodiamonds particularly useful for gene and drug delivery.

4.5. Diamond-nanoparticle-based multifunctional platform for combined targeting, imaging and therapy

Based on the ease of surface modification of nanodiamonds with various functional groups, including targeted probes and drugs, a multifunctional platform for combined targeting, imaging and therapy using diamond nanoparticles has been demonstrated. This combination allows simultaneous diagnosis and therapy and also enables monitoring therapeutic delivery, transport and response. Zhang *et al.* reported the functionalization of nanodiamonds with the hetero-bifunctional cross-linker sulfosuccinimidyl 6-(3'-[2-pyridyldithio]propionamido) hexanoate (sulfo-LC-SPDP) and the subsequent attachment of thiolated antibodies for selective targeting as well as drug-oligonucleotide conjugates, including fluorescein labels and paclitaxel (PTX), for imaging and chemotherapy, respectively, yielding functionalized nanodiamonds abbreviated as PTX-DNA/mAb@NDs, as shown in Fig. 13a.[173] The purpose of the antibody was to target human epidermal growth factor receptor (EGFR), which is overexpressed in many solid tumors, including in lung, colorectal, and breast cancers. PTX is a widely used anticancer drug for breast and ovarian cancers. However, it has several limitations, such as low solubility in water and drug resistance. Commercial formulations of PTX often involve the use of organic solvents that can cause serious side effects; this delivery platform can solve this problem while increasing the bio-availability of PTX. The selective targeting of the nanomedicine was investigated based on cellular uptake by basal EGFR-expressing MCF7 cells and the MDA-MB-231 cell line with EGFR overexpression. The flow cytometry results (Fig. 13b) show that the PTX-DNA/mAb@NDs entered the MDA-MB-231 cells very efficiently because of the overexpression of EGFR, which is specifically targeted by the antibodies on the surfaces of the PTX-DNA/mAb@NDs, in these cells. When PTX-

DNA/mAb@NDs and PTX-DNA@NDs were used, improved cytotoxicity was observed compared with that observed for PTX only. For the MDA-MB-231 cells, the PTX-DNA/mAb@NDs appeared to be the most efficient therapy (Fig. 13c). Overall, these results suggest that PTX-DNA/mAb@NDs can specifically target cells with EGFR overexpression and significantly increase the cellular uptake and therapeutic efficacy of anticancer drugs for these cells. In this example of the use of nanodiamonds in a multimodal application, imaging was achieved through fluorescence labeling instead of using NV^- centers. However, because of the superior advantages of these color centers, it is desirable for future research to focus on nanodiamonds with NV^- centers that can be used for theragnosis. Because of the extremely high photostability of these color centers, it should be possible to achieve precision image-guided therapies.

4.6. Biocompatibility and toxicity of diamond nanoparticles

For the adoption of a new material in practical applications, it is essential to thoroughly investigate that material's biocompatibility and toxicity. For use in clinical settings in particular, it is necessary to understand the absorption, distribution, metabolism and excretion (ADME) characteristics of the material. Because of the superior properties of diamond nanoparticles and their correspondingly high potential for use in a large number of applications, numerous studies have been performed to investigate their biocompatibility and toxicity.

Many experiments have been performed in which various concentrations of diamond nanostructures have been incubated with various cell lines and the resulting viabilities of the cells have been tested. All results indicate that cell viabilities are not negatively affected at reasonably high concentrations of nanodiamonds after 2-3 days of incubation.[58, 59, 174] For example, in the work represented in Fig. 13, over 90% of cells were still alive after incubation with diamond nanoparticles at concentrations of up to 200 μg/ml. Fang *et al.* found that the

internalization of fluorescent diamond nanoparticles did not lead to any significant alteration in the growth and proliferation of HeLa, 3T3-L1 and 489-2.1 cells during 8 days of observation.[175] Following preliminary cytotoxicity investigations of this type in cell lines, many detailed studies have also focused on gaining a full understanding of the influence of nanodiamonds on cell physiology as well as their long-term toxicity in worm and animal models.

Mohan *et al.* performed long-term *in vivo* imaging of diamond nanoparticles in *Caenorhabditis elegans* and investigated their influence on this organism.[61] When bare diamond nanoparticles were used to feed the worms in the absence of *E. coli*, the particles remained in the lumen even at 12 hours after feeding, and there was no uptake of the particles into the intestinal cells. However, when the diamond nanoparticles were surface modified with BSA or carboxymethyldextran (CMDx) before being fed to the worms, the majority of the coated nanoparticles were taken up by the intestinal cells, with very few remaining in the gut lumen region. In addition to these feeding studies, well-dispersed bare diamond nanoparticles were microinjected into the distal gonads of gravid hermaphrodite worms, followed by transfer of the worms to bacterial lawns. Fig. 14a shows the injection site. At 30 min after injection, the nanoparticles were dispersed in the distal gonad and oocytes. The diamond nanoparticles appeared in the cytoplasm of many cells in the early embryos but were predominantly present in the intestinal cells of the late embryos (Fig. 14b and c). This study yielded no evidence that the diamond nanoparticles caused any abnormal embryonic development.[61] In comparison, silica nanoparticles have been found to induce intracorporal hatching of eggs in the parent worms.[176] It was demonstrated that the diamond nanoparticles did not cause any detectable stress to the organism. The diamond-nanoparticle-targeted oocytes could grow in size and become mature oocytes. When these nanoparticle-containing oocytes were fertilized, the resulting embryos developed normally. During the observation period of 14 hours, the

nanoparticles were not excreted from the oocytes or embryos, and no abnormalities were observed during cell division, differentiation, or morphogenesis in embryogenesis.[177]

To further investigate the toxicity of diamond nanoparticles, the lifespan and reproductive potential of worms that were treated with or without either dextran- or BSA-coated diamond nanoparticles were studied. The findings revealed that the lifespan and brood size of the treated and untreated worms were essentially the same.[177] In comparison, silver nanoparticles have been found to affect these parameters and even to result in early death of the organism.[178] Measurements of ROS generation indicated that the diamond nanoparticles did not increase the amount of ROS produced relative to the untreated group.[177] Similarly, Schrand *et al.* also found that nonfluorescent diamond nanoparticles did not increase ROS levels in neuroblastoma cells.[179] To validate these findings that diamond nanoparticles do not generate ROS, further studies need to be performed to find out the reason as it is commonly believed that nanomaterials are capable of producing ROS. This may be very likely to relate to the size, surface chemistry and amount of the used diamond nanoparticles. It is hoped that the study can lead to findings about the control of ROS generation for different purposes.

Following these studies in cell lines and worms, research on the safety of diamond nanoparticles was extended to explorations of the biodistribution of diamond nanoparticles in animal models. Rojas *et al.* used ^{18}F to label nanodiamonds and investigated their distribution using positron emission tomography.[180] The results showed that the nanoparticles were predominantly distributed in the lungs, spleen, and liver and excreted into the urinary tract. The addition of a surfactant such as PEG 8000 or Tween 80 did not significantly alter the pattern of organ uptake but did result in reduced urinary excretion and, correspondingly, increased blood bioavailability[180] Very recently, Zhang *et al.* investigated the *in vivo* biodistribution and clearance of diamond nanoparticles labeled with the near-infrared dye XenoLight CF750 following intravenous injection in mice.[171] By means of whole-body imaging, it was observed

that 3 hours after injection, the nanodiamonds had predominantly accumulated in the liver (Fig. 14d). In comparison, the delivery of free dye led to wide distribution. A quantitative analysis indicated some additional distribution in the spleen, lungs and kidneys (Fig. 14e). The accumulation peaked at 6 hours after injection, and the nanodiamonds had clearly been eliminated after 72 hours. Despite the fact that the nanoparticles predominantly accumulated in the liver, it was found that liver function was not adversely affected, by measuring alanine transferase (ALT), aspartate aminotransferase (AST) and alkaline phosphate (ALP) and performing a histological analysis.

Although most studies have suggested that diamond nanoparticles demonstrate excellent biocompatibility and negligible toxicity, some results have indicated a negative influence of such materials. For example, nanodiamonds with sizes of 4-5 nm were found to lead to increased expression of p53, a DNA repair protein, within 2-4 hours of incubation with mouse embryonic stem cells.[181] An increase in the expression of this protein is commonly observed during the initial stage of DNA damage. With the prolongation of incubation to 24 hours, increased expression of MOGG-1 was observed, indicating the breakage of DNA double strands. Unsurprisingly, the toxicity of nanodiamonds is affected by their surface properties. Oxidized diamond nanoparticles exhibit higher toxicity than do pristine/raw nanoparticles in terms of DNA damage. This has been demonstrated by observations that oxidized nanodiamonds resulted in increased expression of p53 and a higher level of apoptosis compared with pristine/raw nanoparticles. The elevated toxicity was ascribed to either the negatively charged carboxyl groups on the surfaces of the oxidized nanoparticles or the improved cellular uptake of the oxidized nanodiamonds. DNA damage might be caused by nanodiamond-mediated oxidative stress.[182] Vaitkuviene *et al.* found that at low concentrations of up to 100 μg/ml, diamond nanoparticles did not significantly influence the metabolic activity of neuroblastoma SH-SY5Y cells. However, at a higher concentration of 150 μg/ml, the metabolic

activity of the neural cells was dramatically reduced.[183] Despite these observations showing that diamond nanoparticles exhibit slight toxicity, it has been demonstrated that this material causes much less severe DNA damage compared with multi-walled carbon nanotubes (MWCNTs),[181] and it is generally believed that nanodiamonds are more biocompatible and benign than most other nanostructures, including other carbon nanomaterials and semiconductor quantum dots.[184, 185]. This is, in fact, the greatest advantage of diamond nanoparticles, enabling their safe application in drug delivery, imaging and sensing.

5. Vertically aligned diamond nanostructure arrays

5.1. Intracellular drug delivery

The efficient delivery of molecules and materials into living cells is not only essential for scientific studies of cell biology but also greatly useful for the development of novel therapies.[186, 187] Delivering DNA and RNA into cells is necessary for gene therapy.[188, 189] The delivery of fluorescence probes is often needed for cell biology research. The transport of proteins into cells is useful for intervening in cellular processes.[190] Various techniques have been developed for these purposes, including biological, chemical, and physical approaches.[26, 191-197] Among them, physical methods possess unique advantages and are more suitable for certain applications. In particular, micro-injection has been widely and successfully applied to deliver various materials into the cytoplasm and even nuclei of cells.[198, 199] Recently, to improve the throughput of conventional micro-injection, several vertically aligned nanostructure arrays have been demonstrated to act as high-throughput, efficient, and universal intracellular delivery platforms.[200] For example, cells may be cultured on arrays of nanostructures such as silicon nanowires or aluminum oxide nanostraws. During culturing, the nanofeatures slowly penetrate into the cells, thereby enabling the intracellular delivery of molecules and materials such as DNAs, RNAs, peptides, and proteins.[201-205] Different from these approaches, we reported the

use of ultra-small diamond nanoneedle arrays (Fig. 15a and b) for the active disruption of the cell membranes to facilitate the delivery of fluorescent probes and small molecule drugs.[23, 27, 206-208] In our methods, diamond nanoneedle arrays were brought into contact with cells grown on a substrate with a certain force or the cells were applied to the nanoneedles at a relatively fast speed, such that mechanical disruption could be immediately achieved. Early research in this field has been summarized in our previous reviews.[26, 143, 209] Herein, emphasis will be placed on the very recent development of techniques for the delivery of a broader range of molecules and materials to more types of cells, including difficult-to-transfect cells, as well as the *in vivo* application of this type of technique.

Regarding the use of diamond nanoneedle arrays for intracellular delivery, initially, a cell suspension was applied to vertically aligned nanostructures at a fast speed to induce disruption of the cell membranes to facilitate the transport of fluorescent probes or drug molecules into the cells.[208] Later, centrifugation force was employed for precise control of the disruption of the cell membranes by the diamond nanoneedles. In this procedure, cells are cultured on a flat substrate in a well. Before intracellular delivery, the cell culture medium is removed and replaced with a medium containing the molecules or materials to be delivered. Then, a diamond nanoneedle array is introduced, with the needles pointing toward the cells, to cause mechanical disruption of the cell membranes. The disruption is controlled by the centrifugation force, which, in turn, is controlled by tuning the centrifugation speed. After the intracellular delivery process is complete, usually within a few minutes, fresh cell culture medium is added to the well to lift the nanoneedle array off the cells. The scheme is illustrated in Fig. 15c and d.[23] To gain a better understanding of the mechanism by which intracellular transport is facilitated by diamond nanoneedle arrays, the delivery of calcein AM and ethidium homodimer-1 (EthD-1) to fibroblast cells and primary hippocampal neurons was investigated. Calcein AM is membrane permeable, can be cleaved by esterases in live cells, and exhibits green fluorescence.

EthD-1 is membrane impermeable, but it can enter membrane-comprised cells and diffuse to the nucleus, where it emits red fluorescence. Diamond-nanoneedle-treated cells exposed to these agents showed both red and green fluorescence. This indicates that successful cytosolic delivery of EthD-1 through comprised cell membranes can be realized by means of nanoneedle treatment without affecting cell viability. For the delivery of molecules to fibroblast cells and hippocampal neurons, the optimal centrifugation speeds are significantly different, likely because of the differing mechanical properties of the cell membranes. For fibroblast cells, the delivery efficiency of EthD-1 is approximately 5% at 300 rpm (12.8 x *g*, RCF), and it rapidly improves to approximately 80% at 500 rpm (35.5 x *g*). At 300 rpm, the treatment causes negligible cell damage. At 500 to 1000 rpm, the viability of cells still remains at approximately 90%. For neurons, the delivery efficiency of EthD-1 is approximately 80% at a centrifugation speed of 300 rpm. A further increase in speed leads to dramatically increased cell death.

Most attractively, diamond nanoneedle treatment can greatly facilitate the delivery of plasmid DNA into neurons, which are generally very difficult to transfect. The commonly used Lipofectamine transfection method offers a very low transfection efficiency of only 1-5% in primary neurons. Additionally, the protocol often takes several hours because of the endocytosis-based uptake of the DNA complexes. By contrast, with the aid of the diamond nanoneedle treatment of neurons, DNA-lipid complexes are able to enter these cells within a much shorter period of time (5-30 min). A transfection efficiency of approximately 45% can thus be consistently achieved in primary neurons. The method is high in throughput and results in fairly uniform transfection across the entire nanoneedle-array-treated area, as indicated in Fig. 16.[23] The treated cells can still be maintained in long-term culture, allowing proper cellular development and stable GFP expression, as demonstrated by the staining of vesicular glutamate transporter 1 (vGlut1). These results indicate that the diamond nanoneedle treatment of cells is

a powerful method of achieving efficient, high-throughput intracellular delivery, particularly for difficult-to-transfect cell lines.

Similar techniques, although with different materials for the vertical nanostructures, have also recently been used in a variety of applications. For example, carbon nanosyringe arrays have been employed to deliver small interfering RNAs, plasmids, and proteins to difficult-to-transfect cells under centrifugation force.[210] Biodegradable porous silicon nanoneedle arrays have even been used for drug delivery *in vivo*. In that work, human VEGF165 plasmid DNA was delivered to the muscles of mice, and the results were compared with those of the direct injection of the same amount of DNA. Both treatments induced gene expression of human VEGF165 for up to 7 days, but the expression level induced via nanoneedle application was, on average, higher than that induced via direct injection. Moreover, the nanoneedle-treated muscles displayed higher vascularization compared with the control group during two weeks of observation. Consequently, it was concluded that the neovascularization induced via nanoneedle application enables a surge in perfusion, whereas injection has no similar effect. The neovasculature in nanoneedle-treated muscles results in highly interconnected and structured vessels in close proximity to the surface, causing blood perfusion to increase by a factor of six. Evidently, nanoneedle treatment causes new blood vessels to form, with a functional effect. Inspired by these findings, we foresee that our diamond nanoneedle arrays may also be used for highly effective *in vivo* drug delivery in the future. Diamond nanoneedles possess significantly higher mechanical strength than silicon ones; therefore, a diamond-based technique is expected to be more reliable and reproducible and should achieve more consistent outcomes.

5.2. Intracellular sensing

Because nanoneedles can pierce into cells, it would be advantageous to exploit this characteristic for intracellular sensing. Biodegradable porous silicon nanoneedle arrays have been applied to deliver pH-sensitive fluorescein isothiocyanate (FITC), with AlexaFluor 633 (AF633) as a reference, to act as a ratiometric fluorescence sensor. This sensor was tested in the OE33 esophageal adenocarcinoma cell line (cancer cells) and the Het-1A cell line (healthy cells). The intracellular pH values of the OE33 and Het-1A cells were measured to be 6.7 and 7.2, respectively. These results are consistent with those determined via a BCECF ratiometric fluorescence assay.[211] Another example of a potential sensing application of nanoneedles is the intracellular sensing of protein. Cathepsin B (CTSB) is a protease protein that is often confined to the lysosomes and is highly expressed in many tumors.[212] To determine the CTSB expression in cells, a fluorescent dye can be conjugated to nanoneedles using a CTSB-cleavable peptide. If there is CTSB expression in the cells, the peptide will be cleaved, causing the fluorescent dye molecules to be released in the cytosol. Using this method, it is possible to map intracellular CTSB activity in human tissue. In culture, this approach is able to provide single-cell mapping resolution, through which it is possible to distinguish cell phenotypes in mixed culture. These results indicate that nanoneedles show potential for further development for cancer diagnostics. In particular, for Barrett's patients, such a nanoneedle sensor could enable sampling and analysis in the esophageal epithelium during endoscopy, which could make early diagnosis of cancer possible.

Based on a similar principle, the intracellular level of NF-κB can also be determined using diamond nanoneedle arrays. NF-κB is a protein that found in almost all animal cells and is involved in cellular responses to stress or antigens. As a test case, when double-strand DNAs (dsDNA90) enter cells, NF-κB is released because of the activation of stimulator of interferon genes (STING). If the expression of NF-κB is detected, then the innate cellular immunity can be studied by targeting the host-defense response to pathogen molecules. For NF-κB fishing,

DNA aptamers (5′-GGGGAATCCCC-3′) are pre-conjugated to diamond nanoneedles before insertion into cells because they can specifically bind to NF-κB. Fig. 17a shows a schematic of the probing process using diamond nanoneedles inserted into the cell cytoplasm to fish for NF-κB, which is generated upon the stimulation of dsDNA90.[213] The NF-κB signaling dynamics in primary neurons can be studied by means of diamond nanoneedle fishing at various time points (Fig. 17c-d). The results show that the amount of NF-κB present significantly decreases over time after the initial STING activation. At the first instance of probing, the percentage of NF-κB-positive nanoneedles was 52.1±6.7%. This value rapidly decreased to 8.9±0.6% at more than 40 min after the initial delivery of dsDNA90. These results successfully demonstrate that diamond nanoneedle arrays can be conveniently applied to extract the dynamics of signaling components from living cells.

5.3. Biocompatibility and toxicity

For both intracellular delivery and sensing, vertical nanostructures of diamond or a similar material must pierce into cells. Such penetration can be realized by either culturing cells directly on these vertical nanostructure arrays or causing the nanostructures to actively pierce the cell membranes.

Regarding the growth of cells on vertical nanomaterials, a number of studies have been performed to investigate the potential effect on the cells. Despite being impaled on the tips of silicon nanowires, cells can grow and divide over a period of several weeks. SEM images of primary rat hippocampal neurons on silicon nanowires have indicated that these cells can grow and build synaptic connections even with nanostructures penetrating into the neurons. After two weeks of culturing on nanowires, the investigated neurons were still able to fire action potentials upon current injection.[203] However, some cell functions might be perturbed by culturing on such nanostructures for an extended period of time. For example, it has been

discovered that HeLa cells grow slowly and temporarily develop irregular contours when culturing on silicon nanowires and that the penetration of nanowires into the cells leads to lipid scrambling, although this can be reversed in healthy cells.[203] In addition, Persson *et al*. found that if fibroblasts are cultured on vertically aligned nanostructures, cell division will be impaired, and ROS can be generated, leading to DNA damage.[214] It has been reported that when mesenchymal stem cells are grown on vertical silicon nanowire arrays, the adhesion, proliferation and differentiation behaviors of these cells are distinctly different from those of cells grown on flat substrates.[215]

Our studies have shown that when diamond nanoneedle arrays are used for intracellular delivery, this technique does not cause notable cell death compared with untreated cell groups, as confirmed by microscopy observations, MTT assays and measurements of the extracellular level of glucose-6-phosphate dehydrogenase (G6PD).[20, 23, 208] By determining the amount of phosphorylated histone variant H2AX (pH2AX) in the treated cells, it was also found that diamond nanoneedle treatment did not cause double-strand DNA breaks. In this technique, although mechanical disruption to the cell membranes is required to facilitate the entry of materials and molecules into the cells, this disruption is not irreversible. To confirm this, cells were incubated with calcein AM and PI. Calcein AM can be transported into living cells, where it emits green fluorescence. PI does not permeate into living cells and can enter cells only when the cell membrane is comprised. To investigate whether mechanically disrupted cell membranes could recover, these two materials were added to the medium at different time points after the cells were treated with diamond nanoneedle arrays. A group of cells that was not subjected to diamond nanoneedle treatment was used as a control. The results are shown in Fig. 18. When calcein AM and PI were added to the medium immediately after nanoneedle disruption, the intracellular delivery was significantly improved compared with the control group. However, over time, this effect became increasingly weaker. After 40 min, the

intracellular delivery was identical to that in the control group. These observations indicate that cell membranes disrupted by diamond nanoneedles can quickly recover their integrity within a few tens of minutes. In addition to this study, the integrity of the cell membrane at 3, 6, and 24 hours after diamond nanoneedle treatment was further confirmed by means of Image-iT DEAD Green viability stain.

Although diamond nanoneedle treatment causes negligible cell death and double-strand DNA breaks, it does influence the physiology of cells. For example, such treatment can lead to cell apoptosis (Fig. 19).[20] Compared with the untreated group, the population of apoptotic A549 cells increased from 1.31% to 3.17%. When cells were co-treated with both nanoneedles and the anticancer drug cisplatin, the population of apoptotic cells increased from 11.54% to 16.59%. This finding illustrates one of the reasons why the efficacy of cisplatin can be significantly enhanced when cells are also treated with diamond nanoneedles. It was also observed that diamond nanoneedle treatment could lead to elevated intracellular ROS production. However, these negative effects may be partially counteracted by the increase in the intracellular G6PD level that occurs upon nanoneedle treatment. The production of ROS may be induced by the depolarization of the mitochondrial membrane potential caused by the nanoneedles. After depolarization, this potential can slowly recover, reaching its original state by approximately 24 hours after diamond nanoneedle disruption.

6. Conclusions and future outlook

A wide range of nanomaterials have been developed for biomedical applications. To enable their future use in practical applications, it is very important to integrate their various advantages into a single system for optimal performance. Diamond is one such material that possesses collectively superior characteristics and therefore has attracted considerable interest in research on the properties and applications of nanostructures. Diamond nanoparticles that

contain NV^- centers exhibit high absorption, near-infrared emission, ultra-high photostability, no photoblinking, excellent biocompatibility, surface tunability, and intrinsically stable emission, and these characteristics are unaffected by the size, surface modifications or environment of the nanoparticles. By virtue of these characteristics, such nanomaterials are ideal for long-term fluorescence bioimaging and particularly for quantitative analysis. More attractively, NV^- centers are sensitive to magnetic fields, temperatures, ion concentrations, electric fields, and spin densities. Therefore, they can be used as probes to monitor changes in these parameters. In this respect, they show enormous potential to be used for MRI with nanometer resolution under ambient conditions, which would greatly expand the application scope of conventional MRI. The successful development of such technology will provide a powerful tool for studying biological tissues at the molecular level and will enable dramatic advancements in clinical healthcare applications. Vertically aligned diamond nanostructures have recently been applied for high-throughput intracellular delivery and sensing. Compared with chemical and biological techniques for these purposes, this physical tool has considerable advantages. For example, its application is universal, simple, high in throughput, cost-effective and safe and also enables the controllable delivery of materials to specific organelles within cells.

Despite the great progress that has been made in the development of diamond nanomaterials, these materials are far from being ready for practical application. To realize this, great efforts will be required in the following aspects: (1) It is necessary to better understand the surface properties of diamond nanoparticles and their influence on the nanoparticles' functionality and stability in biological environments such as blood because of the potential for interactions with hundreds of proteins. (2) Few studies have investigated the *in vivo* degeneration and fate of diamond nanoparticles. To this end, it is very important to understand their evolution over time in the body and their biodegradation mechanism. (3) Quantitative

studies must be performed to precisely determine the drug loading of diamond nanoparticles and their delivery efficiency to tumors. (4) For MRI specifically, it will be essential to explore means of ensuring the stability of the magnetic properties of NV^- centers when they are located only a few nanometers below the surface, such that their spin properties are maintained. Another necessary future step will be to demonstrate ultra-high resolution MRI in samples of practical importance, such as single protein molecules and living tissues. In addition, NV centers can also be created in vertically aligned diamond nanostructures for intracellular sensing. (5) Given the robust photostability of NV centers, diamond nanoparticles have great potential for use in multipurpose applications such as precision image-guided therapies, and this possibility should be studied. (6) Research on the biocompatibility and toxicity of vertically aligned diamond nanoneedle arrays should be extended to more type of cells, and more physiological parameters need to be explored to understand the possible effects of diamond nanoneedles in a broad range of applications. (7) There is plenty of room for the further development of vertically aligned nanostructures to collect intracellular signals from cells for biological analysis and disease diagnosis. Last but not least, *in vivo* applications of vertically aligned diamond nanostructure arrays should be designed and tested. Because of the remarkable mechanical strength of diamond, when vertically aligned diamond nanostructures are used in applications requiring mechanical force, they are expected to achieve far superior outcomes compared with other types of vertical nanostructures. In this regard, comparative studies should be established, and computer modeling can be employed to explain the differences. These explorations are expected to offer tremendous opportunities to further the development of diamond nanomaterials toward their effective and safe application in drug delivery, bioimaging and biosensing.

Acknowledgement

We are grateful for financial support from the National Science Foundation of China (51372213, and 51672230), and the General Research Fund of Hong Kong (CityU 11338516).

References

1. J. Isberg, J. Hammersberg, E. Johansson, T. Wikstrom, D. J. Twitchen, A. J. Whitehead, S. E. Coe and G. A. Scarsbrook, *Science*, 2002, **297**, 1670-1672.
2. A. M. Zaitsev, *Proc. Natl. Acad. Sci. U. S. A.*, 2008, **105**, 17591-17592.
3. H. K. Tonshoff, H. Hillmann-Apmann and J. Asche, *Diamond Relat. Mater.*, 2002, **11**, 736-741.
4. J. Isberg, J. Hammersberg, D. J. Twitchen and A. Whitehead, *Diamond Relat. Mater.*, 2004, **13**, 320-324.
5. B. A. Fox, M. L. Hartsell, D. M. Malta, H. A. Wynands, G. J. Tessmer and D. L. Dreifus, in *Diamond for Electronic Applications*, eds. D. L. Dreifus, A. Collins, T. Humphreys, K. Das and P. E. Pehrsson, 1996, vol. 416, pp. 319-330.
6. C. S. Yan, Y. K. Vohra, H. K. Mao and R. J. Hemley, *Proc. Natl. Acad. Sci. U. S. A.*, 2002, **99**, 12523-12525.
7. H. Sumiya and S. Satoh, *Diamond Relat. Mater.*, 1996, **5**, 1359-1365.
8. R. S. Balmer, J. R. Brandon, S. L. Clewes, H. K. Dhillon, J. M. Dodson, I. Friel, P. N. Inglis, T. D. Madgwick, M. L. Markham, T. P. Mollart, N. Perkins, G. A. Scarsbrook, D. J. Twitchen, A. J. Whitehead, J. J. Wilman and S. M. Woollard, *J. Phys. Condens. Matter*, 2009, **21**, 364221.
9. C. S. Yan, H. K. Mao, W. Li, J. Qian, Y. S. Zhao and R. J. Hemley, *Phys. Status Solidi a*, 2004, **201**, R25-R27.
10. R. S. Sussmann, J. R. Brandon, S. E. Coe, C. S. J. Pickles, C. G. Sweeney, A. Wasenczuk, C. J. H. Wort and C. N. Dodge, *Ind. Diam. Rev.*, 1998, **58**, 69-77.
11. E. Woerner, C. Wild, W. Mueller-Sebert and P. Koidl, *Diamond and Related Materials*, 2001, **10**, 557-560.
12. N. Govindaraju and R. N. Singh, *Mater. Sci. Eng. B-Adv*, 2011, **176**, 1058-1072.
13. T.-H. Kim, W. M. Choi, D.-H. Kim, M. A. Meitl, E. Menard, H. Jiang, J. A. Carlisle and J. A. Rogers, *Adv. Mater.*, 2008, **20**, 2171-2176.
14. P. Millar, R. B. Birch, A. J. Kemp and D. Burns, *IEEE J. Quant. Electron.*, 2008, **44**, 709-717.
15. A. S. Wilson, *Solid State Technol.*, 2013, **56**, 34-36.
16. K. Kazahaya, A. Yamakawa and T. Fukunisi, *Advances in Abrasive Technology Vi*, 2004, **257-258**, 553-558.
17. M. Willander, M. Friesel, Q. U. Wahab and B. Straumal, *J. Mater. Sci. Mater. Electron.*, 2006, **17**, 1-25.
18. R. B. Vajpayee, P. K. Maharana, N. Sharma, T. Agarwal and V. Jhanji, *J. Cataract Refract. Surg.*, 2014, **40**, 276-282.
19. X. Zhu, M. F. Yuen, L. Yan, Z. Zhang, F. Ai, Y. Yang, P. K. N. Yu, G. Zhu, W. Zhang and X. Chen, *Adv. Healthcare Mater.*, 2016, **5**, 1116-1116.
20. X. Zhu, M. F. Yuen, L. Yan, Z. Zhang, F. Ai, Y. Yang, P. K. N. Yu, G. Zhu, W. Zhang and X. Chen, *Adv. Healthcare Mater.*, 2016, **5**, 1157-1168.
21. V. N. Mochalin, O. Shenderova, D. Ho and Y. Gogotsi, *Nat. Nanotechnol.*, 2012, **7**, 11-23.
22. C. Bradac, T. Gaebel, N. Naidoo, M. J. Sellars, J. Twamley, L. J. Brown, A. S. Barnard, T. Plakhotnik, A. V. Zvyagin and J. R. Rabeau, *Nat. Nanotechnol.*, 2010, **5**, 345-349.
23. Y. Wang, Y. Yang, L. Yan, S. Y. Kwok, W. Li, Z. Wang, X. Zhu, G. Zhu, W. Zhang, X. Chen and P. Shi, *Nat. Commun.*, 2014, **5**, 4466.
24. S. Osswald, G. Yushin, V. Mochalin, S. O. Kucheyev and Y. Gogotsi, *J. Am. Chem. Soc.*, 2006, **128**, 11635-11642.
25. O. Shenderova, A. Koscheev, N. Zaripov, I. Petrov, Y. Skryabin, P. Detkov, S. Turner and G. Van Tendeloo, *J. Phys. Chem. C*, 2011, **115**, 9827-9837.

26. B. He, Y. Yang, M. F. Yuen, X. F. Chen, C. S. Lee and W. J. Zhang, *Nano Today*, 2013, **8**, 265-289.
27. Y. Yang, M.-F. Yuen, X. Chen, S. Xu, Y. Tang and W. Zhang, *Crystengcomm*, 2015, **17**, 2791-2800.
28. G. Balasubramanian, A. Lazariev, S. R. Arumugam and D.-w. Duan, *Curr. Opin. Chem. Biol.*, 2014, **20**, 69-77.
29. J. E. Field, *Rep. Prog. Phys.*, 2012, **75**, 126505.
30. X. Jiang, J. Zhao and X. Jiang, *Nanotechnology*, 2011, **22**, 405705.
31. L. T. Sun, J. L. Gong, D. Z. Zhu, Z. Y. Zhu and S. X. He, *Adv. Mater.*, 2004, **16**, 1849-1853.
32. J. Guo, B. Wen, R. Melnik, S. Yao and T. Li, *Diamond Relat. Mater.*, 2011, **20**, 551-555.
33. O. Shenderova, D. Brenner and R. S. Ruoff, *Nano Lett.*, 2003, **3**, 805-809.
34. A. Kruger, Y. J. Liang, G. Jarre and J. Stegk, *J. Mater. Chem.*, 2006, **16**, 2322-2328.
35. T. Strother, T. Knickerbocker, J. N. Russell, J. E. Butler, L. M. Smith and R. J. Hamers, *Langmuir*, 2002, **18**, 968-971.
36. H. A. Girard, T. Petit, S. Perruchas, T. Gacoin, C. Gesset, J. C. Arnault and P. Bergonzo, *Phys. Chem. Chem. Phys.*, 2011, **13**, 11517-11523.
37. Y. Liang, T. Meinhardt, G. Jarre, M. Ozawa, P. Vrdoljak, A. Schoell, F. Reinert and A. Krueger, *J. Colloid Interface Sci.*, 2011, **354**, 23-30.
38. O. Kuznetsov, Y. Sun, R. Thaner, A. Bratt, V. Shenoy, M. S. Wong, J. Jones and W. E. Billups, *Langmuir*, 2012, **28**, 5243-5248.
39. A. Kruger, F. Kataoka, M. Ozawa, T. Fujino, Y. Suzuki, A. E. Aleksenskii, A. Y. Vul and E. Osawa, *Carbon*, 2005, **43**, 1722-1730.
40. A. Krueger, J. Stegk, Y. Liang, L. Lu and G. Jarre, *Langmuir*, 2008, **24**, 4200-4204.
41. A. Krueger and T. Boedeker, *Diamond Relat. Mater.*, 2008, **17**, 1367-1370.
42. Y. Liu, Z. N. Gu, J. L. Margrave and V. N. Khabashesku, *Chem. Mater.*, 2004, **16**, 3924-3930.
43. A. Nagl, S. R. Hemelaar and R. Schirhagl, *Anal. Bioanal. Chem.*, 2015, **407**, 7521-7536.
44. K. Ushizawa, Y. Sato, T. Mitsumori, T. Machinami, T. Ueda and T. Ando, *Chem. Phys. Lett.*, 2002, **351**, 105-108.
45. D. Mitev, R. Dimitrova, M. Spassova, C. Minchev and S. Stavrev, *Diamond Relat. Mater.*, 2007, **16**, 776-780.
46. A. Krueger and D. Lang, *Adv. Funct. Mater.*, 2012, **22**, 890-906.
47. L. Rondin, G. Dantelle, A. Slablab, F. Grosshans, F. Treussart, P. Bergonzo, S. Perruchas, T. Gacoin, M. Chaigneau, H. C. Chang, V. Jacques and J. F. Roch, *Phys. Rev. B*, 2010, **82**, 115449.
48. Y. Liu, V. N. Khabashesku and N. J. Halas, *J. Am. Chem. Soc.*, 2005, **127**, 3712-3713.
49. W.-W. Zheng, Y.-H. Hsieh, Y.-C. Chiu, S.-J. Cai, C.-L. Cheng and C. Chen, *J. Mater. Chem.*, 2009, **19**, 8432-8441.
50. M. Schvartzman and S. J. Wind, *Nanotechnology*, 2009, **20**, 145306.
51. B. V. Spitsyn, S. A. Denisov, N. A. Skorik, A. G. Chopurova, S. A. Parkaeva, L. D. Belyakova and O. G. Larionov, *Diamond Relat. Mater.*, 2010, **19**, 123-127.
52. M.-H. Hsu, H. Chuang, F.-Y. Cheng, Y.-P. Huang, C.-C. Han, J.-Y. Chen, S.-C. Huang, J.-K. Chen, D.-S. Wu, H.-L. Chu and C.-C. Chang, *ACS Appl. Mater. Interfaces*, 2014, **6**, 7198-7203.
53. A. Krueger, *Chem. Eur. J.*, 2008, **14**, 1382-1390.
54. A. Krueger, *J. Mater. Chem.*, 2008, **18**, 1485-1492.
55. A. M. Derfus, W. C. W. Chan and S. N. Bhatia, *Nano Lett.*, 2004, **4**, 11-18.
56. A. Hoshino, K. Fujioka, T. Oku, M. Suga, Y. F. Sasaki, T. Ohta, M. Yasuhara, K. Suzuki and K. Yamamoto, *Nano Lett.*, 2004, **4**, 2163-2169.
57. C. Kirchner, T. Liedl, S. Kudera, T. Pellegrino, A. M. Javier, H. E. Gaub, S. Stolzle, N. Fertig and W. J. Parak, *Nano Lett.*, 2005, **5**, 331-338.
58. M. Chen, E. D. Pierstorff, R. Lam, S.-Y. Li, H. Huang, E. Osawa and D. Ho, *ACS Nano*, 2009, **3**, 2016-2022.
59. J. Xiao, X. Duan, Q. Yin, Z. Zhang, H. Yu and Y. Li, *Biomaterials*, 2013, **34**, 9648-9656.
60. C. Y. Fang, V. Vaijayanthimala, C. A. Cheng, S. H. Yeh, C. F. Chang, C. L. Li and H. C. Chang, *Small*, 2011, **7**, 3363-3370.

61. N. Mohan, C.-S. Chen, H.-H. Hsieh, Y.-C. Wu and H.-C. Chang, *Nano Lett.*, 2010, **10**, 3692-3699.
62. J.-L. Li, B. Tang, B. Yuan, L. Sun and X.-G. Wang, *Biomaterials*, 2013, **34**, 9519-9534.
63. S. Chinnathambi, S. Chen, S. Ganesan and N. Hanagata, *Adv. Healthcare Mater.*, 2014, **3**, 10-29.
64. X. H. Gao, Y. Y. Cui, R. M. Levenson, L. W. K. Chung and S. M. Nie, *Nat. Biotechnol.*, 2004, **22**, 969-976.
65. M. Bates, B. Huang, G. T. Dempsey and X. Zhuang, *Science*, 2007, **317**, 1749-1753.
66. M. Lan, J. Zhang, X. Zhu, P. Wang, X. Chen, C.-S. Lee and W. Zhang, *Nano Res.*, 2015, **8**, 2380-2389.
67. J. Yu, X. Zhang, X. Hao, X. Zhang, M. Zhou, C.-S. Lee and X. Chen, *Biomaterials*, 2014, **35**, 3356-3364.
68. X. Hao, M. Zhou, X. Zhang, J. Yu, J. Jie, C. Yu and X. Zhang, *Chem. Commun.*, 2014, **50**, 737-739.
69. J. Yu, X. Diao, X. Zhang, X. Chen, X. Hao, W. Li, X. Zhang and C.-S. Lee, *Small*, 2014, **10**, 1125-1132.
70. L. Yan, Y. Wang, J. Li, S. Kalytchuk, A. S. Susha, S. V. Kershaw, F. Yan, A. L. Rogach and X. Chen, *J. Mater. Chem. C*, 2014, **2**, 4490-4494.
71. P. Alivisatos, *Nat. Biotechnol.*, 2004, **22**, 47-52.
72. Y. Chen, H. Chen and J. Shi, *Adv. Mater.*, 2013, **25**, 3144-3176.
73. F. Erogbogbo, K.-T. Yong, I. Roy, G. Xu, P. N. Prasad and M. T. Swihart, *ACS Nano*, 2008, **2**, 873-878.
74. B. F. P. McVey and R. D. Tilley, *Acc. Chem. Res.*, 2014, **47**, 3045-3051.
75. F. Peng, Y. Su, Y. Zhong, C. Fan, S.-T. Lee and Y. He, *Acc. Chem. Res.*, 2014, **47**, 612-623.
76. Y. He, Z.-H. Kang, Q.-S. Li, C. H. A. Tsang, C.-H. Fan and S.-T. Lee, *Angew. Chem. Int. Ed.*, 2009, **48**, 128-132.
77. Y. Zhong, F. Peng, F. Bao, S. Wang, X. Ji, L. Yang, Y. Su, S.-T. Lee and Y. He, *J. Am. Chem. Soc.*, 2013, **135**, 8350-8356.
78. Y. He, C. Fan and S.-T. Lee, *Nano Today*, 2010, **5**, 282-295.
79. Y. Wang and A. Hu, *J. Mater. Chem. C*, 2014, **2**, 6921-6939.
80. X. Ren, J. Liu, X. Meng, J. Wei, T. Liu and F. Tang, *Chem. Asian J.*, 2014, **9**, 1054-1059.
81. G. Balasubramanian, I. Y. Chan, R. Kolesov, M. Al-Hmoud, J. Tisler, C. Shin, C. Kim, A. Wojcik, P. R. Hemmer, A. Krueger, T. Hanke, A. Leitenstorfer, R. Bratschitsch, F. Jelezko and J. Wrachtrup, *Nature*, 2008, **455**, 648-651.
82. D. Rugar, H. J. Mamin, M. H. Sherwood, M. Kim, C. T. Rettner, K. Ohno and D. D. Awschalom, *Nat. Nanotechnol.*, 2015, **10**, 120-124.
83. M. S. Grinolds, M. Warner, K. De Greve, Y. Dovzhenko, L. Thiel, R. L. Walsworth, S. Hong, P. Maletinsky and A. Yacoby, *Nat. Nanotechnol.*, 2014, **9**, 279-284.
84. X. Chen, C. Zou, Z. Gong, C. Dong, G. Guo and F. Sun, *Light Sci. Appl.*, 2015, **4**, e230.
85. S. J. Yu, M. W. Kang, H. C. Chang, K. M. Chen and Y. C. Yu, *J. Am. Chem. Soc.*, 2005, **127**, 17604-17605.
86. Y.-R. Chang, H.-Y. Lee, K. Chen, C.-C. Chang, D.-S. Tsai, C.-C. Fu, T.-S. Lim, Y.-K. Tzeng, C.-Y. Fang, C.-C. Han, H.-C. Chang and W. Fann, *Nat. Nanotechnol.*, 2008, **3**, 284-288.
87. S. C. Lawson, D. Fisher, D. C. Hunt and M. E. Newton, *J. Phys. Condens. Matter*, 1998, **10**, 6171-6180.
88. T.-L. Wee, Y.-K. Tzeng, C.-C. Han, H.-C. Chang, W. Fann, J.-H. Hsu, K.-M. Chen and Y.-C. Yull, *J. Phys. Chem. A*, 2007, **111**, 9379-9386.
89. P. G. Baranov, A. A. Soltamova, D. O. Tolmachev, N. G. Romanov, R. A. Babunts, F. M. Shakhov, S. V. Kidalov, A. Y. Vul, G. V. Mamin, S. B. Orlinskii and N. I. Silkin, *Small*, 2011, **7**, 1533-1537.
90. C.-C. Fu, H.-Y. Lee, K. Chen, T.-S. Lim, H.-Y. Wu, P.-K. Lin, P.-K. Wei, P.-H. Tsao, H.-C. Chang and W. Fann, *Proc. Natl. Acad. Sci. U. S. A.*, 2007, **104**, 727-732.
91. C.-W. Chang, D. Sud and M.-A. Mycek, in *Methods in Cell Biology*, eds. G. Sluder and D. E. Wolf, 2007, vol. 81, pp. 495-524.

92. W. W.-W. Hsiao, Y. Y. Hui, P.-C. Tsai and H.-C. Chang, *Acc. Chem. Res.*, 2016, **49**, 400-407.
93. R. Schirhagl, K. Chang, M. Loretz and C. L. Degen, in *Annual Review of Physical Chemistry, Vol 65*, eds. M. A. Johnson and T. J. Martinez, 2014, vol. 65, pp. 83-105.
94. R. Chapman and T. Plakhotnik, *Chem. Phys. Lett.*, 2011, **507**, 190-194.
95. N. Mohan, Y.-K. Tzeng, L. Yang, Y.-Y. Chen, Y. Y. Hui, C.-Y. Fang and H.-C. Chang, *Adv. Mater.*, 2010, **22**, 843-847.
96. Y. Y. Hui, L. J. Su, O. Y. Chen, Y. T. Chen, T. M. Liu and H. C. Chang, *Sci. Rep.*, 2014, **4**, 5574.
97. J. Wang, D. X. Ye, G. H. Liang, J. Chang, J. L. Kong and J. Y. Chen, *J. Mater. Chem. B*, 2014, **2**, 4338-4345.
98. G. Vicidomini, G. Moneron, K. Y. Han, V. Westphal, H. Ta, M. Reuss, J. Engelhardt, C. Eggeling and S. W. Hell, *Nat. Methods*, 2011, **8**, 571-573.
99. A. Gruber, A. Drabenstedt, C. Tietz, L. Fleury, J. Wrachtrup and C. vonBorczyskowski, *Science*, 1997, **276**, 2012-2014.
100. W. van Sark, P. Frederix, D. J. Van den Heuvel, H. C. Gerritsen, A. A. Bol, J. N. J. van Lingen, C. D. Donega and A. Meijerink, *J. Phys. Chem. B*, 2001, **105**, 8281-8284.
101. W. van Sark, P. Frederix, A. A. Bol, H. C. Gerritsen and A. Meijerink, *Chemphyschem*, 2002, **3**, 871-879.
102. W. Wang, C. Damm, J. Walter, T. J. Nacken and W. Peukert, *Phys. Chem. Chem. Phys.*, 2016, **18**, 466-475.
103. J. Wrachtrup, *Nat. Nanotechnol.*, 2010, **5**, 314-315.
104. X. Chen, J. L. Hutchison, P. J. Dobson and G. Wakefield, *J. Mater. Sci.*, 2009, **44**, 285-292.
105. P. K. Sharma, R. K. Dutta, C. H. Liu, R. Pandey and A. C. Pandey, *Mater. Lett.*, 2010, **64**, 1183-1186.
106. Z. Y. Zhou, L. Brus and R. Friesner, *Nano Lett.*, 2003, **3**, 163-167.
107. G. Allan, C. Delerue and M. Lannoo, *Phys. Rev. Lett.*, 1996, **76**, 2961-2964.
108. I. P. Chang, K. C. Hwang and C.-S. Chiang, *J. Am. Chem. Soc.*, 2008, **130**, 15476-15481.
109. J. Gong, N. Steinsultz and M. Ouyang, *Nat. Commun.*, 2016, **7**, 11820-11820.
110. Y. Il Park, K. T. Lee, Y. D. Suh and T. Hyeon, *Chem. Soc. Rev.*, 2015, **44**, 1302-1317.
111. L. Wei, P. Zhou, Q. X. Yang, Q. Y. Yang, M. Ma, B. Chen and L. H. Xiao, *Nanoscale*, 2014, **6**, 11351-11358.
112. B. Bruhn, J. Valenta, F. Sangghaleh and J. Linnros, *Nano Lett.*, 2011, **11**, 5574-5580.
113. D. S. English, L. E. Pell, Z. H. Yu, P. F. Barbara and B. A. Korgel, *Nano Lett.*, 2002, **2**, 681-685.
114. O. Faklaris, D. Garrot, V. Joshi, J.-P. Boudou, T. Sauvage, P. A. Curmi and F. Treussart, *J. Eur. Opt. Soc. Rapid*, 2009, **4**, 09035.
115. C. P. Epperla, N. Mohan, C.-W. Chang, C.-C. Chen and H.-C. Chang, *Small*, 2015, **11**, 6097-6105.
116. W. Liu, F. Yu, J. Yang, B. Xiang, P. Xiao and L. Wang, *Adv. Funct. Mater.*, 2016, **26**, 365-375.
117. Y.-K. Tzeng, O. Faklaris, B.-M. Chang, Y. Kuo, J.-H. Hsu and H.-C. Chang, *Angew. Chem. Int. Ed.*, 2011, **50**, 2262-2265.
118. K. Y. Han, K. I. Willig, E. Rittweger, F. Jelezko, C. Eggeling and S. W. Hell, *Nano Lett.*, 2009, **9**, 3323-3329.
119. S. Arroyo-Camejo, M.-P. Adam, M. Besbes, J.-P. Hugonin, V. Jacques, J.-J. Greffet, J.-F. Roch, S. W. Hell and F. Treussart, *ACS Nano*, 2013, **7**, 10912-10919.
120. E. Rittweger, K. Y. Han, S. E. Irvine, C. Eggeling and S. W. Hell, *Nat. Photonics*, 2009, **3**, 144-147.
121. H.-H. Lin, H.-W. Lee, R.-J. Lin, C.-W. Huang, Y.-C. Liao, Y.-T. Chen, J.-M. Fang, T.-C. Lee, A. L. Yu and H.-C. Chang, *Small*, 2015, **11**, 4394-4402.
122. X. Jiang, C. Rocker, M. Hafner, S. Brandholt, R. M. Dorlich and G. U. Nienhaus, *ACS Nano*, 2010, **4**, 6787-6797.
123. S. Ohta, S. Inasawa and Y. Yamaguchi, *Biomaterials*, 2012, **33**, 4639-4645.
124. N. Zhou, S. Zhu, S. Maharjan, Z. Hao, Y. Song, X. Zhao, Y. Jiang, B. Yang and L. Lu, *RSC Adv.*, 2014, **4**, 62086-62095.

125. K. Arai, C. Belthangady, H. Zhang, N. Bar-Gill, S. J. DeVience, P. Cappellaro, A. Yacoby and R. L. Walsworth, *Nat. Nanotechnol.*, 2015, **10**, 859-864.
126. S. J. DeVience, L. M. Pham, I. Lovchinsky, A. O. Sushkov, N. Bar-Gill, C. Belthangady, F. Casola, M. Corbett, H. Zhang, M. Lukin, H. Park, A. Yacoby and R. L. Walsworth, *Nat. Nanotechnol.*, 2015, **10**, 129-134.
127. C. Mueller, X. Kong, J. M. Cai, K. Melentijevic, A. Stacey, M. Markham, D. Twitchen, J. Isoya, S. Pezzagna, J. Meijer, J. F. Du, M. B. Plenio, B. Naydenov, L. P. McGuinness and F. Jelezko, *Nat. Commun.*, 2014, **5**, 4703.
128. D. Le Sage, K. Arai, D. R. Glenn, S. J. DeVience, L. M. Pham, L. Rahn-Lee, M. D. Lukin, A. Yacoby, A. Komeili and R. L. Walsworth, *Nature*, 2013, **496**, 486-489.
129. A. Boretti, L. Rosa and S. Castelletto, *Small*, 2015, **11**, 4229-4236.
130. H. J. Mamin, M. Kim, M. H. Sherwood, C. T. Rettner, K. Ohno, D. D. Awschalom and D. Rugar, *Science*, 2013, **339**, 557-560.
131. P. Maletinsky, S. Hong, M. S. Grinolds, B. Hausmann, M. D. Lukin, R. L. Walsworth, M. Loncar and A. Yacoby, *Nat. Nanotechnol.*, 2012, **7**, 320-324.
132. T. Staudacher, F. Shi, S. Pezzagna, J. Meijer, J. Du, C. A. Meriles, F. Reinhard and J. Wrachtrup, *Science*, 2013, **339**, 561-563.
133. N. Zhao, J. Honert, B. Schmid, M. Klas, J. Isoya, M. Markham, D. Twitchen, F. Jelezko, R.-B. Liu, H. Fedder and J. Wrachtrup, *Nat. Nanotechnol.*, 2012, **7**, 657-662.
134. L. P. McGuinness, Y. Yan, A. Stacey, D. A. Simpson, L. T. Hall, D. Maclaurin, S. Prawer, P. Mulvaney, J. Wrachtrup, F. Caruso, R. E. Scholten and L. C. L. Hollenberg, *Nat. Nanotechnol.*, 2011, **6**, 358-363.
135. F. C. Ziem, N. S. Goetz, A. Zappe, S. Steinert and J. Wrachtrup, *Nano Lett.*, 2013, **13**, 4093-4098.
136. S. Steinert, F. Ziem, L. T. Hall, A. Zappe, M. Schweikert, N. Goetz, A. Aird, G. Balasubramanian, L. Hollenberg and J. Wrachtrup, *Nat. Commun.*, 2013, **4**, 1607.
137. L. T. Hall, G. C. G. Beart, E. A. Thomas, D. A. Simpson, L. P. McGuinness, J. H. Cole, J. H. Manton, R. E. Scholten, F. Jelezko, J. Wrachtrup, S. Petrou and L. C. L. Hollenberg, *Sci. Rep.*, 2012, **2**, 401.
138. S. Kaufmann, D. A. Simpson, L. T. Hall, V. Perunicic, P. Senn, S. Steinert, L. P. McGuinness, B. C. Johnson, T. Ohshima, F. Caruso, J. Wrachtrup, R. E. Scholten, P. Mulvaney and L. Hollenberg, *Proc. Natl. Acad. Sci. U. S. A.*, 2013, **110**, 10894-10898.
139. L. T. Hall, C. D. Hill, J. H. Cole, B. Staedler, F. Caruso, P. Mulvaney, J. Wrachtrup and L. C. L. Hollenberg, *Proc. Natl. Acad. Sci. U. S. A.*, 2010, **107**, 18777-18782.
140. A. Ermakova, G. Pramanik, J. M. Cai, G. Algara-Siller, U. Kaiser, T. Weil, Y. K. Tzeng, H. C. Chang, L. P. McGuinness, M. B. Plenio, B. Naydenov and F. Jelezko, *Nano Lett.*, 2013, **13**, 3305-3309.
141. G. Kucsko, P. C. Maurer, N. Y. Yao, M. Kubo, H. J. Noh, P. K. Lo, H. Park and M. D. Lukin, *Nature*, 2013, **500**, 54-58.
142. Y.-K. Tzeng, P.-C. Tsai, H.-Y. Liu, O. Y. Chen, H. Hsu, F.-G. Yee, M.-S. Chang and H.-C. Chang, *Nano Lett.*, 2015, **15**, 3945-3952.
143. L. Yan, J. Zhang, C.-S. Lee and X. Chen, *Small*, 2014, **10**, 4487-4504.
144. J. Zhang, Y. Li, F.-F. An, X. Zhang, X. Chen and C.-S. Lee, *Nano Lett.*, 2015, **15**, 313-318.
145. J. Zhang, Y.-C. Liang, X. Lin, X. Zhu, L. Yan, S. Li, X. Yang, G. Zhu, A. L. Rogach, P. K. N. Yu, P. Shi, L.-C. Tu, C.-C. Chang, X. Zhang, X. Chen, W. Zhang and C.-S. Lee, *ACS Nano*, 2015, **9**, 9741-9756.
146. R. Gupta, J. Shea, C. Scafe, A. Shurlygina and N. Rapoport, *J. Control. Release*, 2015, **212**, 70-77.
147. N. Rapoport, R. Gupta, Y.-S. Kim and B. E. O'Neill, *J. Control. Release*, 2015, **206**, 153-160.
148. T. H. L. Kim, H. Jun, J. S. Kim and Y. S. Nam, *J. Colloid Interface Sci.*, 2015, **443**, 197-205.
149. R. Lam and D. Ho, *Expert Opin. Drug Deliv.*, 2009, **6**, 883-895.
150. Z. Zhang, B. Niu, J. Chen, X. He, X. Bao, J. Zhu, H. Yu and Y. Li, *Biomaterials*, 2014, **35**, 4565-4572.

151. E. K. Chow, X.-Q. Zhang, M. Chen, R. Lam, E. Robinson, H. Huang, D. Schaffer, E. Osawa, A. Goga and D. Ho, *Sci. Transl. Med.*, 2011, **3**, 73ra21.
152. G. Xi, E. Robinson, B. Mania-Farnell, E. F. Vanin, K.-W. Shim, T. Takao, E. V. Allender, C. S. Mayanil, M. B. Soares, D. Ho and T. Tomita, *Nanomedicine: NBM*, 2014, **10**, 381-391.
153. H. B. Man, H. Kim, H.-J. Kim, E. Robinson, W. K. Liu, E. K.-H. Chow and D. Ho, *Nanomedicine: NBM*, 2014, **10**, 359-369.
154. X. Wang, X. C. Low, W. Hou, L. N. Abdullah, T. B. Toh, M. M. A. Rashid, D. Ho and E. K.-H. Chow, *ACS Nano*, 2014, **8**, 12151-12166.
155. Z. Cui, Y. Zhang, J. Zhang, H. Kong, X. Tang, L. Pan, K. Xia, A. Aldalbahi, A. Li, R. Tai, C. Fan and Y. Zhu, *Carbon*, 2016, **97**, 78-86.
156. H. Wang, D.-K. Lee, K.-Y. Chen, J.-Y. Chen, K. Zhang, A. Silva, C.-M. Ho and D. Ho, *ACS Nano*, 2015, **9**, 3332-3344.
157. M. I. Setyawati, V. N. Mochalin and D. T. Leong, *ACS Nano*, 2016, **10**, 1170-1181.
158. L. Yan, Z. J. Gu and Y. L. Zhao, *Chem. Asian J.*, 2013, **8**, 2342-2353.
159. M. I. Setyawati, C. Y. Tay and D. T. Leong, *Biomaterials*, 2013, **34**, 10133-10142.
160. D.-K. Lee, S. V. Kim, A. N. Limansubroto, A. Yen, A. Soundia, C.-Y. Wang, W. Shi, C. Hong, S. Tetradis, Y. Kim, N.-H. Park, M. K. Kang and D. Ho, *ACS Nano*, 2015, **9**, 11490-11501.
161. T.-K. Ryu, R.-H. Kang, K.-Y. Jeong, D.-R. Jun, J.-M. Koh, D. Kim, S. K. Bae and S.-W. Choi, *J. Control. Release*, 2016, **232**, 152-160.
162. Y. Wong, K. Markham, Z. P. Xu, M. Chen, G. Q. Lu, P. F. Bartlett and H. M. Cooper, *Biomaterials*, 2010, **31**, 8770-8779.
163. K. Ladewig, M. Niebert, Z. P. Xu, P. P. Gray and G. Q. M. Lu, *Biomaterials*, 2010, **31**, 1821-1829.
164. L. Feng, S. Zhang and Z. Liu, *Nanoscale*, 2011, **3**, 1252-1257.
165. X. Wang, K. Liu, G. Yang, L. Cheng, L. He, Y. Liu, Y. Li, L. Guo and Z. Liu, *Nanoscale*, 2014, **6**, 9198-9205.
166. R. Martin, M. Alvaro, J. R. Herance and H. Garcia, *ACS Nano*, 2010, **4**, 65-74.
167. X.-Q. Zhang, M. Chen, R. Lam, X. Xu, E. Osawa and D. Ho, *ACS Nano*, 2009, **3**, 2609-2616.
168. M. Chen, X. Q. Zhang, H. B. Man, R. Lam, E. K. Chow and D. A. Ho, *J. Phys. Chem. Lett.*, 2010, **1**, 3167-3171.
169. J.-R. Bertrand, C. Pioche-Durieu, J. Ayala, T. Petit, H. A. Girard, C. P. Malvy, E. Le Cam, F. Treussart and J.-C. Arnault, *Biomaterials*, 2015, **45**, 93-98.
170. A. Alhaddad, M. P. Adam, J. Botsoa, G. Dantelle, S. Perruchas, T. Gacoin, C. Mansuy, S. Lavielle, C. Malvy, F. Treussart and J. R. Bertrand, *Small*, 2011, **7**, 3087-3095.
171. Y. Zhang, Z. Cui, H. Kong, K. Xia, L. Pan, J. Li, Y. Sun, J. Shi, L. Wang, Y. Zhu and C. Fan, *Adv. Mater.*, 2016, **28**, 2699-2708.
172. Z. Chu, K. Miu, P. Lung, S. Zhang, S. Zhao, H.-C. Chang, G. Lin and Q. Li, *Sci. Rep.*, 2015, **5**, 11661.
173. X.-Q. Zhang, R. Lam, X. Xu, E. K. Chow, H.-J. Kim and D. Ho, *Adv. Mater.*, 2011, **23**, 4770-4775.
174. L. Zhao, Y.-H. Xu, T. Akasaka, S. Abe, N. Komatsu, F. Watari and X. Chen, *Biomaterials*, 2014, **35**, 5393-5406.
175. C.-Y. Fang, V. Vaijayanthimala, C.-A. Cheng, S.-H. Yeh, C.-F. Chang, C.-L. Li and H.-C. Chang, *Small*, 2011, **7**, 3363-3370.
176. A. Pluskota, E. Horzowski, O. Bossinger and A. von Mikecz, *Plos One*, 2009, **4(8)**, e6622.
177. Y. Kuo, T.-Y. Hsu, Y.-C. Wu and H.-C. Chang, *Biomaterials*, 2013, **34**, 8352-8360.
178. J.-y. Roh, S. J. Sim, J. Yi, K. Park, K. H. Chung, D.-y. Ryu and J. Choi, *Environ. Sci. Technol.*, 2009, **43**, 3933-3940.
179. A. M. Schrand, H. Huang, C. Carlson, J. J. Schlager, E. Osawa, S. M. Hussain and L. Dai, *J. Phys. Chem. B*, 2007, **111**, 2-7.
180. S. Rojas, J. D. Gispert, R. Martin, S. Abad, C. Menchon, D. Pareto, V. M. Victor, M. Alvaro, H. Garcia and J. Raul Herance, *ACS Nano*, 2011, **5**, 5552-5559.
181. Y. Xing, W. Xiong, L. Zhu, E. Osawa, S. Hussin and L. Dai, *ACS Nano*, 2011, **5**, 2376-2384.
182. N. Dworak, M. Wnuk, J. Zebrowski, G. Bartosz and A. Lewinska, *Carbon*, 2014, **68**, 763-776.

183. A. Vaitkuviene, V. Ratautaite, A. Ramanaviciene, K. Sanen, R. Paesen, M. Ameloot, V. Petrakova, M. McDonald, F. Vahidpour, V. Kaseta, G. Ramanauskaite, G. Biziuleviciene, M. Nesladek and A. Ramanavicius, *MCP*, 2015, **29**, 25-30.
184. J. Bartelmess, S. J. Quinn and S. Giordani, *Chem. Soc. Rev.*, 2015, **44**, 4672-4698.
185. K. E. Zakrzewska, A. Samluk, M. Wierzbicki, S. Jaworski, M. Kutwin, E. Sawosz, A. Chwalibog, D. G. Pijanowska and K. D. Pluta, *Plos One*, 2015, **10(3)**, e0122579.
186. E. M. Chan, S. Ratanasirintrawoot, I. H. Park, P. D. Manos, Y. H. Loh, H. G. Huo, J. D. Miller, O. Hartung, J. Rho, T. A. Ince, G. Q. Daley and T. M. Schlaeger, *Nat. Biotechnol.*, 2009, **27**, 1033-1037.
187. K.-Y. Pu, K. Li, J. Shi and B. Liu, *Chem. Mater.*, 2009, **21**, 3816-3822.
188. A. A. Eltoukhy, D. Chen, O. Veiseh, J. M. Pelet, H. Yin, Y. Dong and D. G. Anderson, *Biomaterials*, 2014, **35**, 6454-6461.
189. H.-X. Wang, X.-Z. Yang, C.-Y. Sun, C.-Q. Mao, Y.-H. Zhu and J. Wang, *Biomaterials*, 2014, **35**, 7622-7634.
190. D. S. D'Astolfo, R. J. Pagliero, A. Pras, W. R. Karthaus, H. Clevers, V. Prasad, R. J. Lebbink, H. Rehmann and N. Geijsen, *Cell*, 2015, **161**, 674-690.
191. A. Sharei, J. Zoldan, A. Adamo, W. Y. Sim, N. Cho, E. Jackson, S. Mao, S. Schneider, M.-J. Han, A. Lytton-Jean, P. A. Basto, S. Jhunjhunwala, J. Lee, D. A. Heller, J. W. Kang, G. C. Hartoularos, K.-S. Kim, D. G. Anderson, R. Langer and K. F. Jensen, *Proc. Natl. Acad. Sci. U. S. A.*, 2013, **110**, 2082-2087.
192. L. Yan, W. Chen, X. Zhu, L. Huang, Z. Wang, G. Zhu, V. A. L. Roy, K. N. Yu and X. Chen, *Chem. Commun.*, 2013, **49**, 10938-10940.
193. C. Yu, M. Zhou, X. Zhang, W. Wei, X. Chen and X. Zhang, *Nanoscale*, 2015, **7**, 5683-5690.
194. J. Peng, M. A. Garcia, J.-s. Choi, L. Zhao, K.-J. Chen, J. R. Bernstein, P. Peyda, Y.-S. Hsiao, K. W. Liu, W.-Y. Lin, A. D. Pyle, H. Wang, S. Hou and H.-R. Tseng, *ACS Nano*, 2014, **8**, 4621-4629.
195. A. Bertucci, H. Luelf, D. Septiadi, A. Manicardi, R. Corradini and L. De Cola, *Adv. Healthcare Mater.*, 2014, **3**, 1812-1817.
196. T. Thambi, D. G. You, H. S. Han, V. G. Deepagan, S. M. Jeon, Y. D. Suh, K. Y. Choi, K. Kim, I. C. Kwon, G.-R. Yi, J. Y. Lee, D. S. Lee and J. H. Park, *Adv. Healthcare Mater.*, 2014, **3**, 1829-1838.
197. P. Verderio, S. Avvakumova, G. Alessio, M. Bellini, M. Colombo, E. Galbiati, S. Mazzucchelli, J. P. Avila, B. Santini and D. Prosperi, *Adv. Healthcare Mater.*, 2014, **3**, 957-976.
198. W. Wang, Y. Sun, M. Zhang, R. Anderson, L. Langille and W. Chan, *Rev. Sci. Instrum.*, 2008, **79(10)**, 104302.
199. L. Y. T. Chou, K. Ming and W. C. W. Chan, *Chem. Soc. Rev.*, 2011, **40**, 233-245.
200. S. Park, Y. S. Kim, W. B. Kim and S. Jon, *Nano Lett.*, 2009, **9**, 1325-1329.
201. W. Kim, J. K. Ng, M. E. Kunitake, B. R. Conklin and P. Yang, *J. Am. Chem. Soc.*, 2007, **129**, 7228-7229.
202. J. J. VanDersarl, A. M. Xu and N. A. Melosh, *Nano Lett.*, 2012, **12**, 3881-3886.
203. A. K. Shalek, J. T. Robinson, E. S. Karp, J. S. Lee, D.-R. Ahn, M.-H. Yoon, A. Sutton, M. Jorgolli, R. S. Gertner, T. S. Gujral, G. MacBeath, E. G. Yang and H. Park, *Proc. Natl. Acad. Sci. U. S. A.*, 2010, **107**, 1870-1875.
204. A. M. Xu, A. Aalipour, S. Leal-Ortiz, A. H. Mekhdjian, X. Xie, A. R. Dunn, C. C. Garner and N. A. Melosh, *Nat. Commun.*, 2014, **5**, 3613.
205. X. Xie, A. M. Xu, S. Leal-Ortiz, Y. H. Cao, C. C. Garner and N. A. Melosh, *ACS Nano*, 2013, **7**, 4351-4358.
206. X. Zhu, S. Y. Kwok, M. F. Yuen, L. Yan, W. Chen, Y. Yang, Z. Wang, K. N. Yu, G. Zhu, W. Zhang and X. Chen, *J. Mater. Sci.*, 2015, **50**, 7800-7807.
207. E. Y. W. Chong, C. Y. P. Ng, V. W. Y. Choi, L. Yan, Y. Yang, W. J. Zhang, K. W. K. Yeung, X. F. Chen and K. N. Yu, *J. Mater. Chem. B*, 2013, **1**, 3390-3396.
208. X. Chen, G. Zhu, Y. Yang, B. Wang, L. Yan, K. Y. Zhang, K. K.-W. Lo and W. Zhang, *Adv. Healthcare Mater.*, 2013, **2**, 1103-1107.
209. L. Yan, Y. Yang, W. Zhang and X. Chen, *Adv. Mater.*, 2014, **26**, 5533-5540.

210. M. Choi, S. H. Lee, W. B. Kim, V. Gujrati, D. Kim, J. Lee, J. Kim, H. Kim, P. E. Saw and S. Jon, *Adv. Healthcare Mater.*, 2015, **5**, 101-107.
211. C. Chiappini, J. O. Martinez, E. De Rosa, C. S. Almeida, E. Tasciotti and M. M. Stevens, *ACS Nano*, 2015, **9**, 5500-5509.
212. C. Chiappini, P. Campagnolo, C. S. Almeida, N. Abbassi-Ghadi, L. W. Chow, G. B. Hanna and M. M. Stevens, *Adv. Mater.*, 2015, **27**, 5147-5152.
213. Z. Wang, Y. Yang, Z. Xu, Y. Wang, W. Zhang and P. Shi, *Nano Lett.*, 2015, **15**, 7058-7063.
214. H. Persson, C. Kobler, K. Molhave, L. Samuelson, J. O. Tegenfeldt, S. Oredsson and C. N. Prinz, *Small*, 2013, **9**, 4006-4016.
215. D. Liu, C. Yi, K. Wang, C.-C. Fong, Z. Wang, P. K. Lo, D. Sun and M. Yang, *ACS Appl. Mater. Interfaces*, 2013, **5**, 13295-13304.

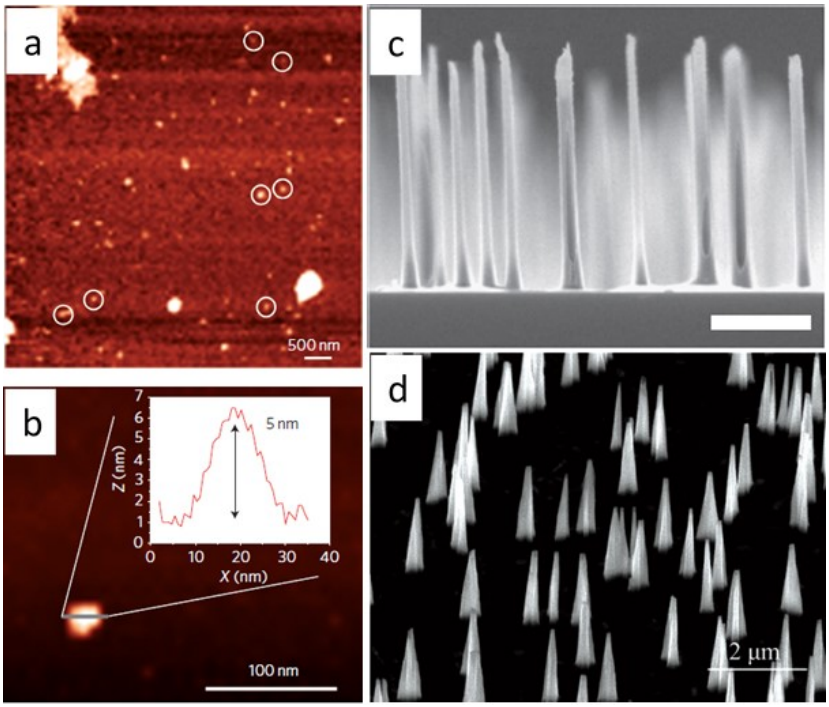

Fig. 1 a. Characterisation of discrete 5-nm diamonds on a glass coverslip; b. Magnified AFM image and corresponding surface profile (inset) of a representative nanocrystal 5 nm in height;[22] c and d. SEM images of vertically diamond nanoneedle arrays (The scale bar in c indicates 2 µm).[20, 23]

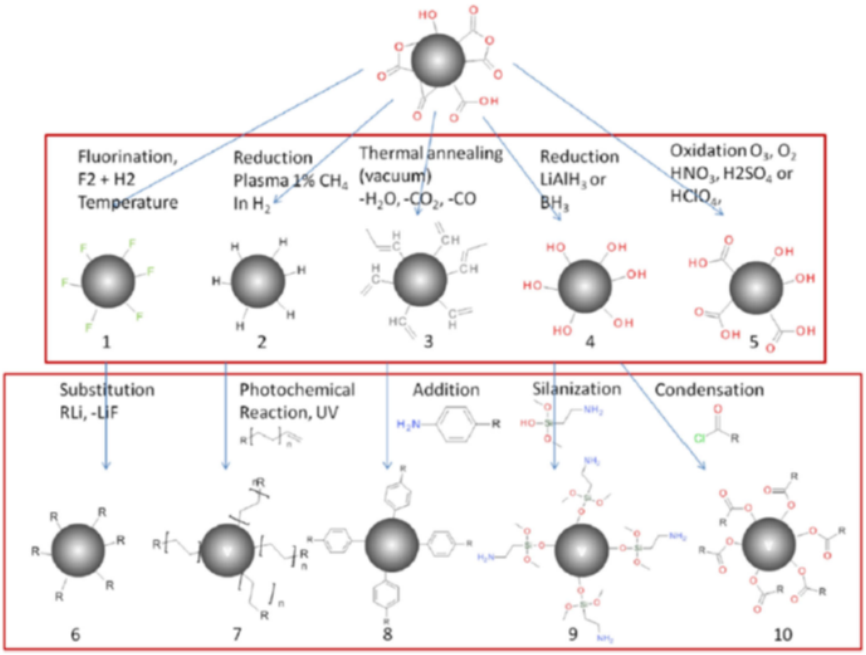

Fig. 2 Overview of the most important surface modification methods for covalently attaching molecules to diamond: The upper half shows different first steps that are performed to provide a homogeneous surface. Details on the synthesis for the different surface terminations can be found in the respective references: 1[34], 2[35, 36], 3[37, 38], 4[34], 5[39]. The lower half shows different ways of attaching a linker molecule (R stands for the desired functional groups, e.g., NH_2): 6[42], 7[35, 36], 8[37], 9[34, 40], 10[41].

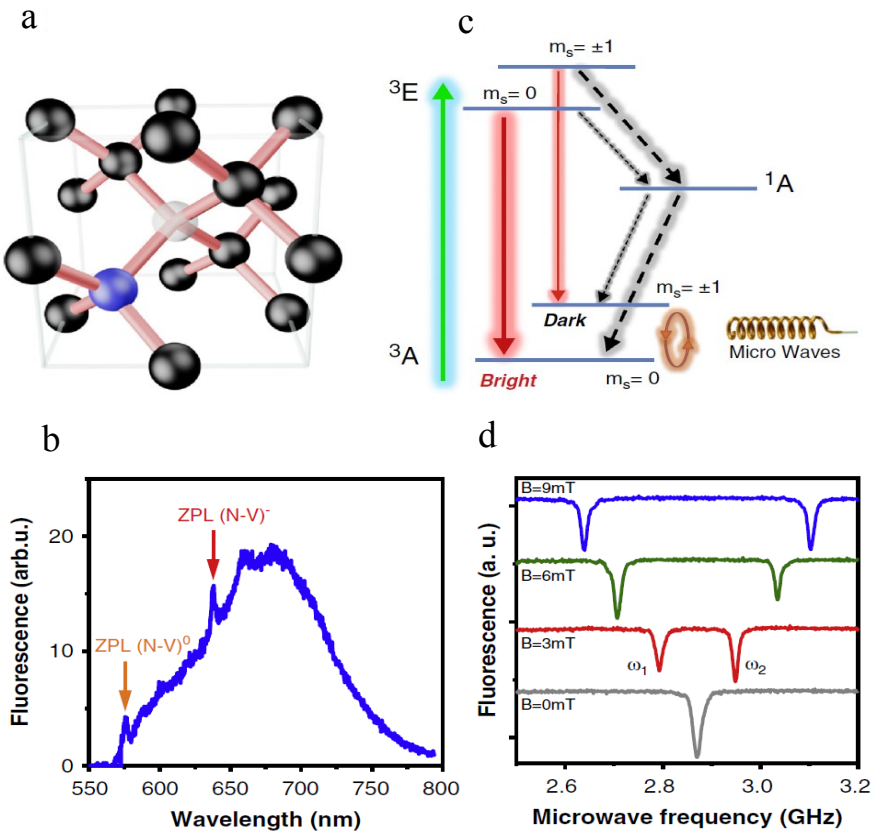

Fig. 3 (a) The atomic structure of a single Nitrogen-Vacancy (NV) defect in diamond. Substituted Nitrogen atom (blue) bound to Vacancy site (white) in a diamond lattice (black). (b) Fluorescence emission from single NV defect showing zero-phonon-lines (ZPL) of NV^- and NV^0 characteristics. (c) Energy level structure of NV defect and the spin sublevels optical excitation 532 nm (green arrow), Fluorescence emission (red arrows 637–750 nm) non-radiative decay processes (black dashed lines) and orange lines spin transitions driven by MW fields. (d) Optically detected Magnetic resonance (ODMR) spectrum of single NV spin and the corresponding Zeeman effect on magnetic field dependence.[28]

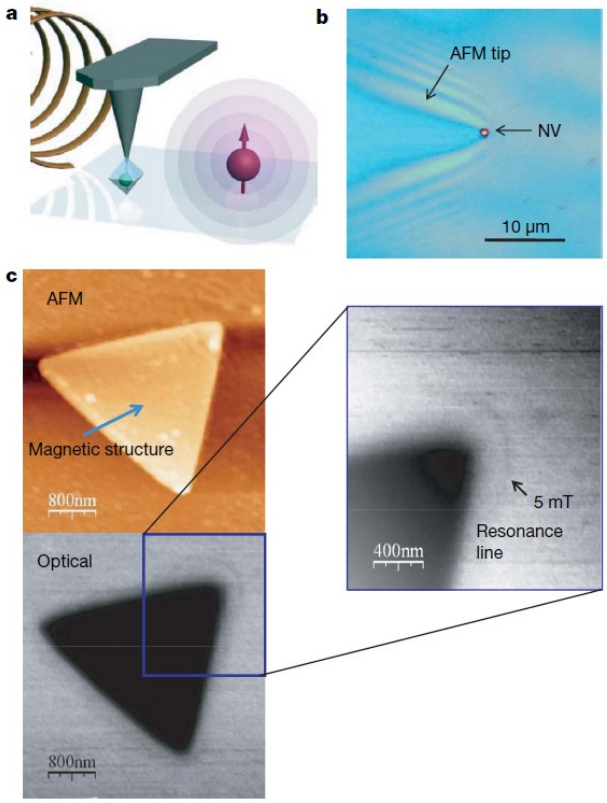

Fig. 4 Scanning probe magnetometry. (a) Diagram of the magnetic field imaging experiment. A nanoscale magnetic particle (red) is imaged with a single nitrogen-vacancy defect (green, within the blue nanocrystal) fixed at the scanning probe tip (black). (b) Optical image of a diamond nanocrystal attached to an AFM tip (view from the bottom). The scattered light image of the tip is overlapped with the fluorescence image of the nanocrystal. The bright spot (arrowed) represents fluorescence of a single nitrogen-vacancy defect. Fluorescence autocorrelation function (data not shown) shows a pronounced antibunching dip, indicating a single nitrogen-vacancy defect in the nanocrystal on the AFM tip. (c) Field reconstruction using the scanning probe single spin magnetometer. Top left, an AFM image of a nickel magnetic nanostructure prepared by electron beam lithography; bottom left, a magneto-optical image of the same structure, recorded using a single nitrogen-vacancy centre on the AFM tip as light source and magnetometer. Inset (right), the fluorescence signal from the scanned nitrogen-vacancy centre attached to the apex of the AFM tip when resonant microwaves at 2,750 MHz are applied (the arrowed point corresponds to 5mT resonance line with the magnetic field tilted by 45º relative to the nitrogen-vacancy axis).[81]

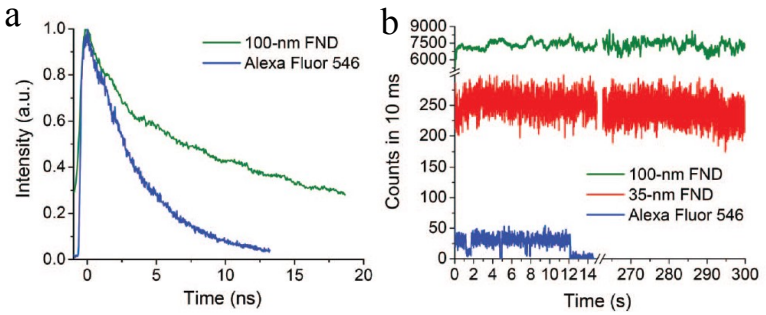

Fig. 5 Characterization of single fluorescence nanodiamonds (FNDs). (a) Fluorescence lifetime measurements of 100-nm FNDs (green) and Alexa Fluor 546 dye molecules (blue). Fitting the time traces with two exponential decays reveals a fast component of 1.7 ns (4%) and a slow component of 17 ns (96%). The latter is four times longer than that (≈4 ns) of Alexa Fluor 546. (b) Typical time traces of the fluorescence from a single 100-nm FND (green), a single 35-nm FND (red), and a single Alexa Fluor 546 dye molecule attached to a single dsDNA molecule (blue). Note that no sign of photobleaching was detected within 300 s of the continuous excitation for the FNDs.[90]

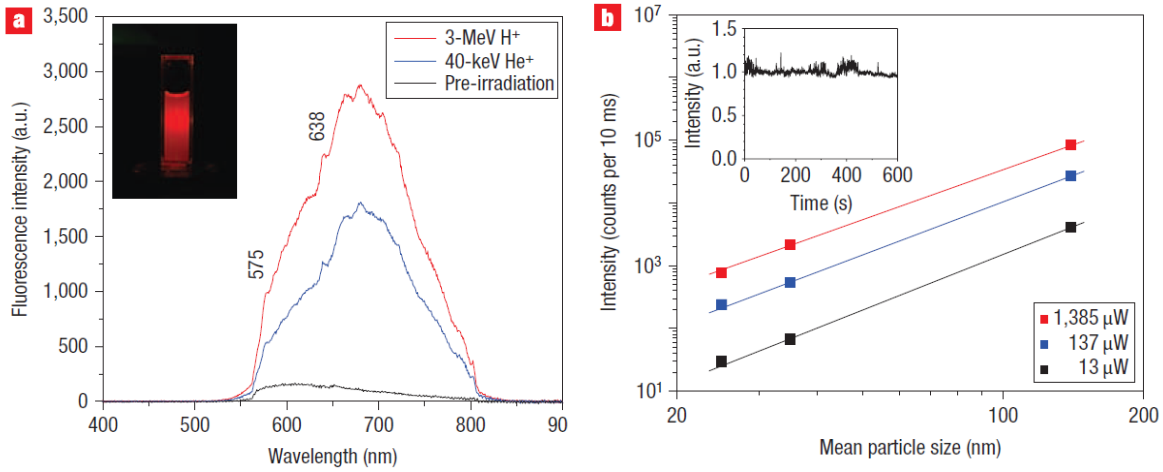

Fig. 6 Characterization of fluorescent nanodiamonds (FNDs). (a) Fluorescence spectra of 35-nm FNDs suspended in water (1 mg ml^{-1} each), prepared with either 40-keV He^{+} or 3-MeV H^{+} irradiation. Inset: Fluorescence image of a 35-nm FND suspension excited by 532-nm laser light. (b) Fluorescence intensities of FNDs as a function of particle size at three different laser powers. Each data point is the mean of measurements for more than 15 different FNDs. The slopes of the linear fits vary from 2.65 to 2.95 over the power range used in the measurements. Inset: Fluorescence time trace (intensity normalized) of a 25-nm FND.[80]

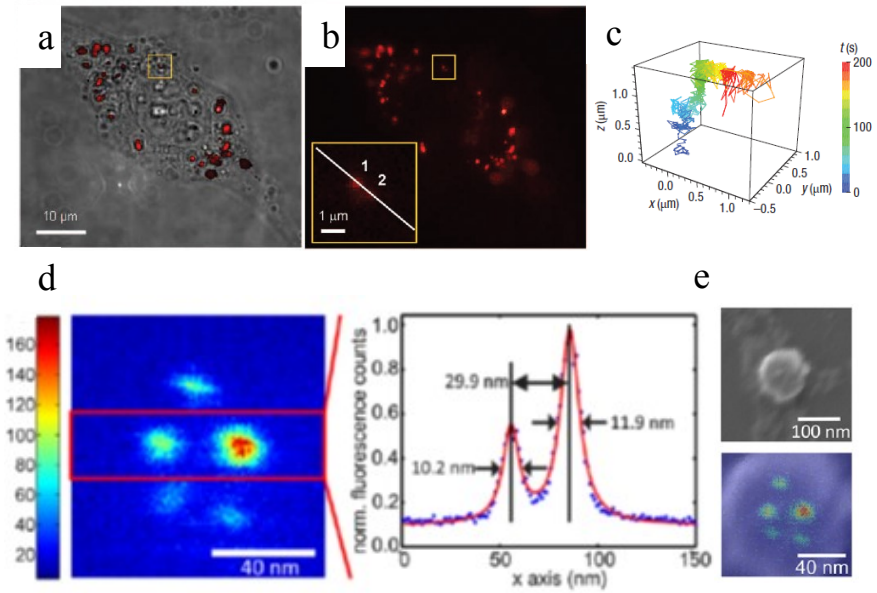

Fig. 7 Observation of single FNDs in a HeLa cell. (a) Bright-field and epifluorescence images of a HeLa cell after uptake of 35-nm FNDs. Most of the uptaken FNDs are seen to distribute in the cytoplasm.[90] (b) Epifluorescence image of a single HeLa cell after the FND uptake. An enlarged view of the fluorescence spots (denoted by ‘‘1’’ and ‘‘2’’) with diffraction-limited sizes (FWHM ≈ 500 nm) is shown in *Inset*. The separation between these two particles is ≈1 μm.[90] (d) Three-dimensional trajectory (shown in pseudo-colour, right panel) and displacements of a single FND inside a cell over a time span of 200 s.[86] (d) Subdiffraction resolution STED image and corresponding vertically binned STED image profile of a diamond particle with ~ 100 nm diameter showing five isolated NV^- centres (red curve: Lorentzian fit). (e) SEM image of the same nanodiamond and overlay of the STEM image and the SEM image illustrating the relative dimensions.[119]

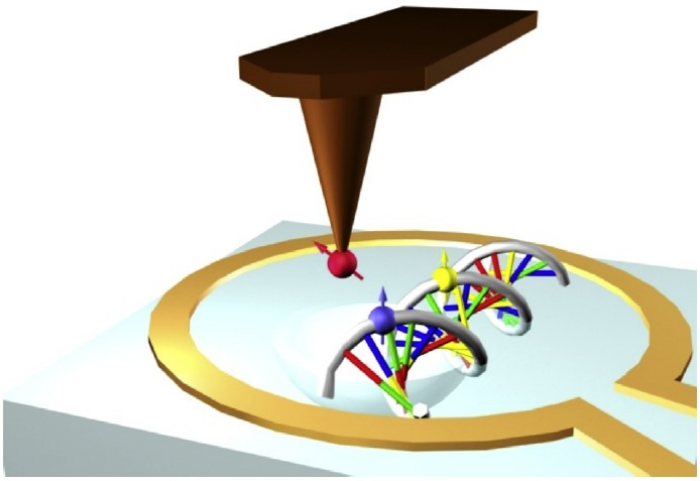

Fig. 8 The schematic representation of a molecular structure microscope. The NV spin sensor is scanned relative to the biomolecule either in the manner shown above or in swapped configuration. Spin density can be effectively mapped at various locations to reconstruct the molecular structure of isolated biomolecules in three dimensions.[28]

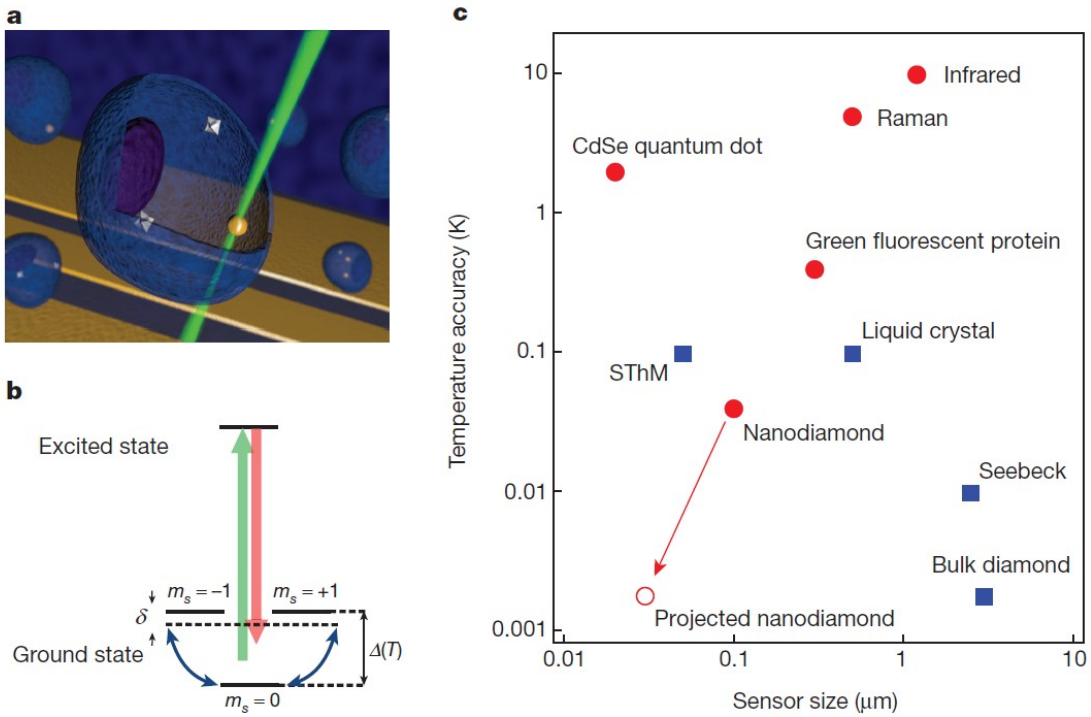

Fig. 9 Nitrogen–vacancy-based nanoscale thermometry. a, Schematic image depicting nanodiamonds (grey diamonds) and a gold nanoparticle (yellow sphere) within a living cell (central blue object; others are similar) with coplanar waveguide (yellow stripes) in the background. The controlled application of local heat is achieved by laser illumination of the gold nanoparticle, and nanoscale thermometry is achieved by precision spectroscopy of the nitrogen–vacancy spins in the nanodiamonds. b, Simplified nitrogen–vacancy level diagram showing a ground-state spin triplet and an excited state. At zero magnetic field, the $|\pm1\rangle$ sublevels are split from the $|0\rangle$ state by a temperature-dependent zero field splitting $\Delta(T)$. Pulsed microwave radiation is applied (detuning, δ) to perform Ramsey-type spectroscopy. c, Comparison of sensor sizes and temperature accuracies for the nitrogen–vacancy quantum thermometer and other reported techniques. Red circles indicate methods that are biologically compatible. The open red circle indicates the ultimate expected accuracy for our measurement technique in solution.[141]

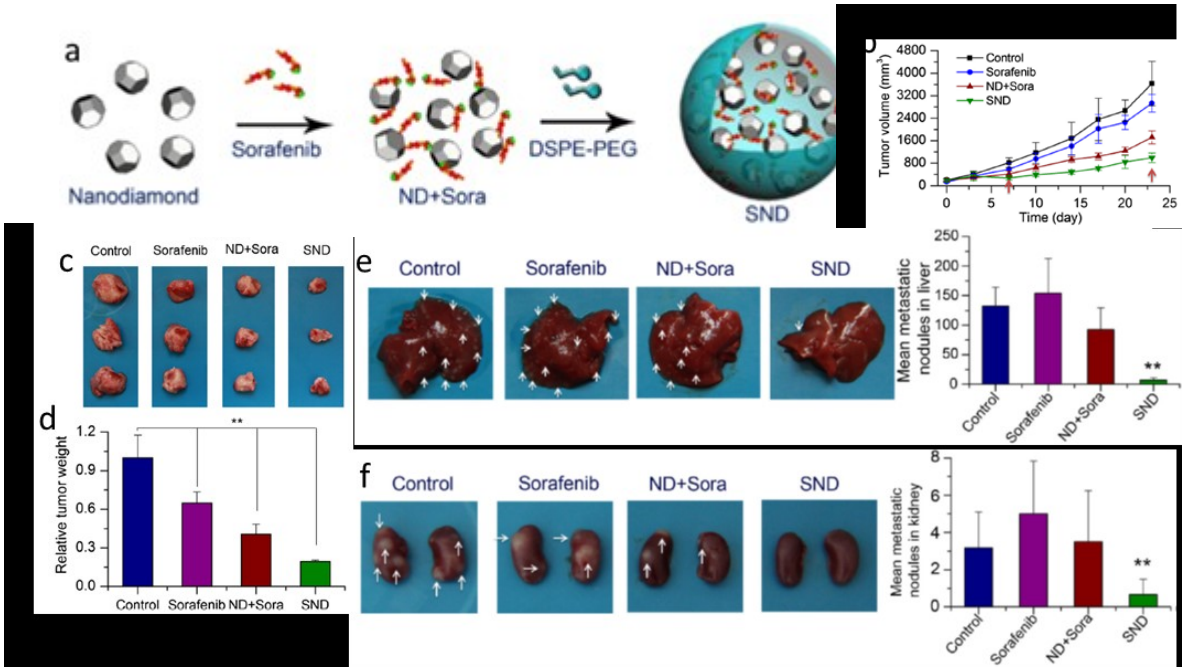

Fig. 10 a: Illustration of the preparation of lipid-coated diamond nanoparticle clusters loaded with water insoluble sorafenib. b, c, and d Tumour growth inhibition effects in BGC-823 gastric cancer cells induced tumour xeograft mice (20 mg/kg). b: The relative tumour volumes in tumour xenograft models treated with saline, sorafenib suspension, nanodiamond (ND) + sorafenib (Sora) and lipid-coated diamond nanoclusters loaded with sorafenib (SND) by oral gavage (20 mg/kg). c: The photographs of tumours from each group excised on day 23 after oral administration. d: The relative tumour weight in mice with treatment of sorafenib, ND + Sora and SND in comparison with saline group (**$p < 0.01$). e and f: Therapeutic efficacy of SND on suppressing the distant metastasis to liver (e) and kidney (f) in BGC-823 gastric cancer cells induced tumour xenograft mice. Mice were daily treated with saline, sorafenib suspension, ND + Sora and SND at 20 mg/kg of sorafenib by oral gavage. At the end point, the visually detected metastatic nodules in each tissue of liver and kidney were counted.[150]

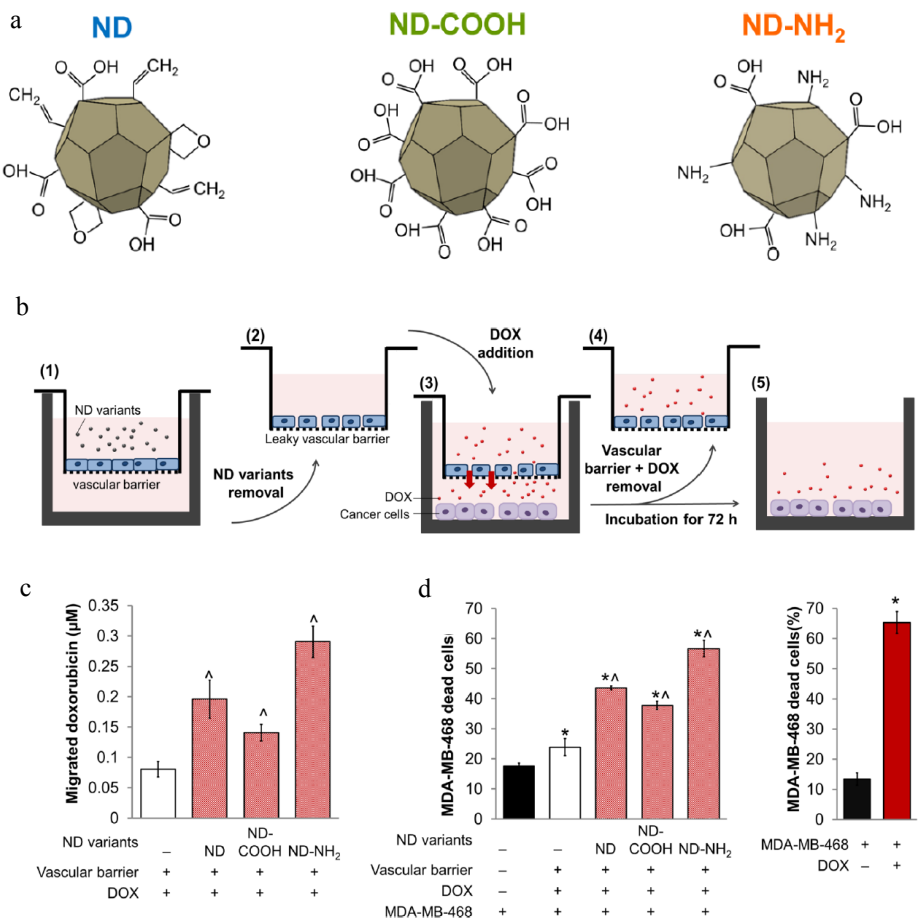

Fig. 11 (a) Schematic representation of nanodiamond (ND) variants surface characteristic. (b-d): ND-induced vascular barrier leakiness assists cancer therapy by promoting penetration of cancer drug across the vascular barrier. (b): Experimental scheme. (1) Vascular barrier was treated with ND variants to induce leakiness. (2) Following the induction of leakiness the ND variants were removed and the leaky vascular barrier was transferred to another well in which the MDA-MB-468 cancer cells were grown and (3) the doxorubicin (DOX) was added. (4) The excess DOX was removed along with the EC, followed by quantification of the amount of DOX successfully penetrating the vascular barrier and the DOX effect on the MDA-MD-468. (c): ND variant treatments promotes the penetration of DOX across the vascular barrier. (d): Increase cancer cell (MDA-MB-468) cytotoxicity concomitant with the increase of DOX penetration over leaky vascular barrier. Fresh cell culture medium and DOX (320 nM) were added to single culture MDA-MB-468 cells to serve as negative and positive controls, respectively. Data are means ± S.D., n = 3, Student's t-test, $p < 0.05$, ^Significant against untreated vascular barrier. *Significant against untreated MDA-MB-468 group.[157]

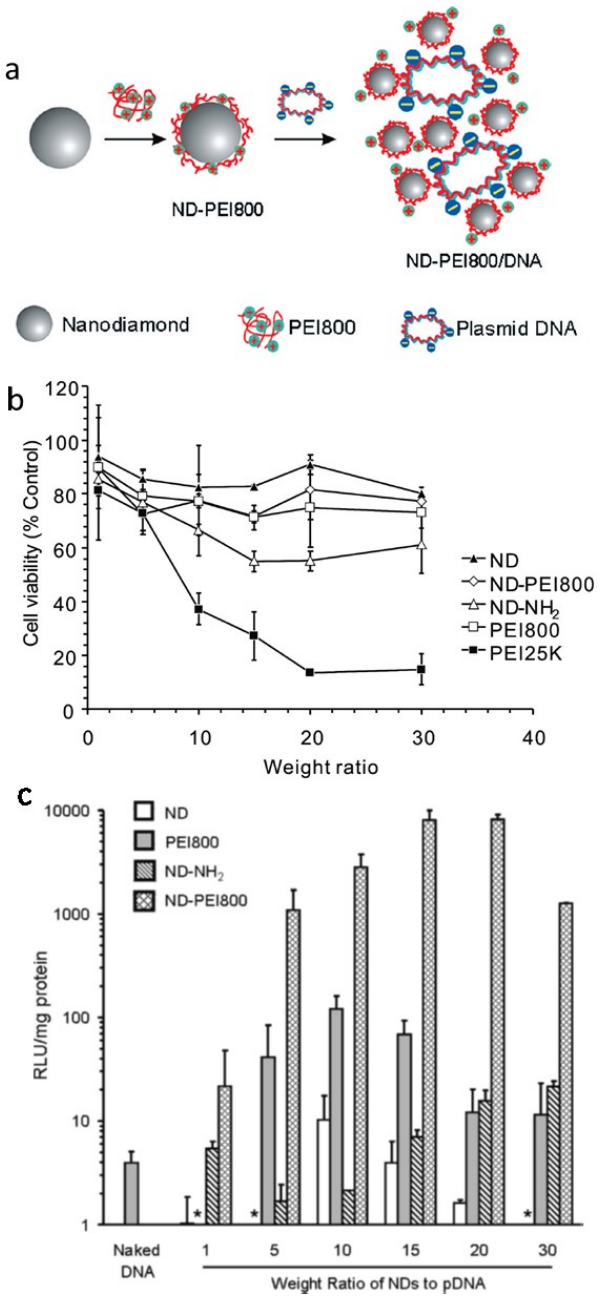

Fig. 12 a. Illustration of using PEI800 surface-modified nanodiamond (ND) for DNA delivery. b. Cytotoxicity assay of HeLa cultures with complexes formed by different carriers with pDNA at weight ratios from 1 to 30. c. ND-PEI800-mediated pLuc transfection in HeLa cells induces greatest pLuc expression. Maximum transfection efficiency was observed at a weight ratio of 20 for ND-PEI800. Note the low transfection efficiency of ND alone and PEI800 alone compared to the ND-PEI800 vector. Data is represented as a mean ± standard deviation (N = 2). An asterisk denotes particles with transfection efficiency lower than 1 RLU/mg of protein in the cell lysate.[167]

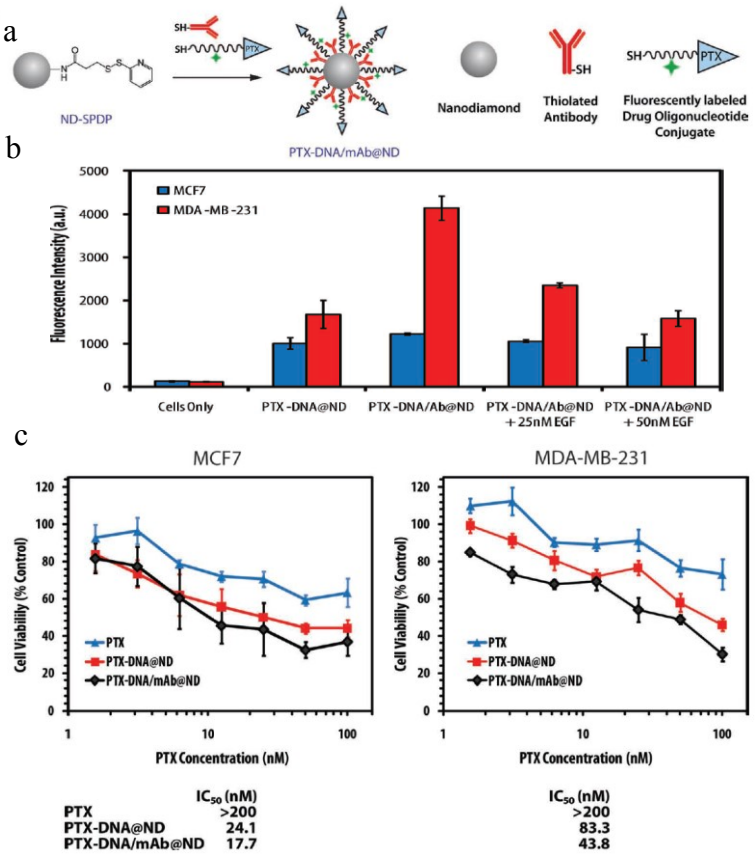

Fig. 13 (a) Synthetic scheme of multifunctional PTX-DNA/mAb@nanodiamonds (NDs). Sulfo-LC-SPDP was attached on to an aminated ND surface (ND-NH_2), forming sulfhydryl-reactive NDs (ND-SPDPs). Thiolated drug-oligonucleotide conjugates and thiolated mAbs were then simultaneously attached to ND-SPDPs. (b) Quantitative analysis of PTX-DNA@ND and PTX-DNA/mAb@ND internalization within cells. Flow cytometry analysis of fluorescein-labeled oligonucleotides is representative of ND-conjugate internalization into MCF7 and MDA-MB-231 cells. Data is represented as the mean ±standard deviation (N = 2). (c) Cytotoxicity profi les of PTX (blue triangles), PTX-DNA@NDs (red squares) and PTX-DNA/mAb@NDs (black diamonds) in respect to escalating equivalent PTX doses in MCF7 and MDA-MB-231 cells after 48 h incubation (n = 6). Corresponding IC 50 values are listed underneath.[173]

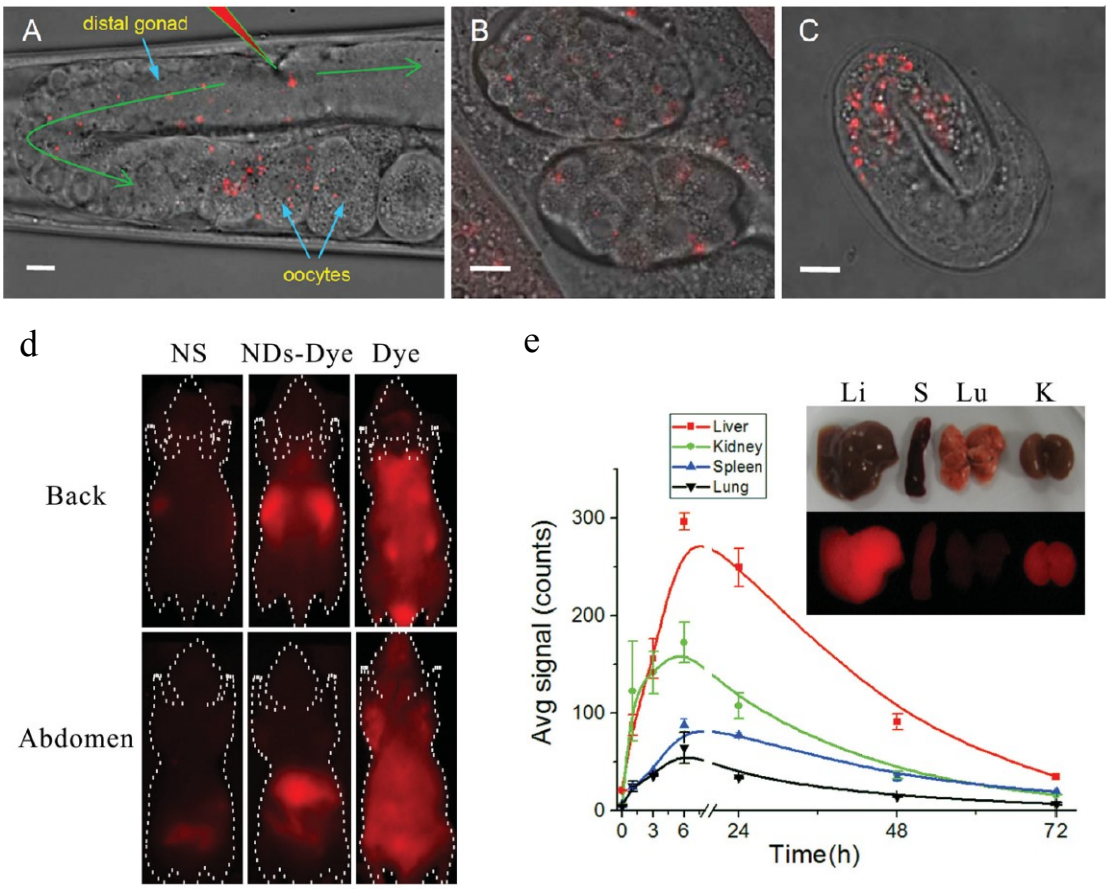

Fig. 14 Microinjection of bare fluorescence nanodiamonds (FNDs) into C. elegans. (A-C) Epifluorescence/DIC-merged images of an injected worm (A) and its progeny at the early (B) and late (C) embryonic stages. The FNDs dispersed in the distal gonad and oocytes at approximately 30 min after injection (A). Green arrows indicate bulk streaming of FNDs with cytoplasmic materials and the red triangle indicates the site of injection. Note that the injected FNDs are present in the cytoplasm of many cells in the early embryos (B) but predominantly in the intestinal cells of the late embryo (C). Scale bars are 10 μm.[61] (D) representative whole-body images of ICR mice after tail vein administration with 1.2 mg of XenoLight CF750-labeled NDs or 30 fmol of XenoLight 750 (NS: normal silane; ND: nanodiamond). (E) quantification of NDs accumulated in mouse tissues at different time points after tail vein administration with XenoLight 750-labeled NDs with a dose of 80 μg per mouse (20 g) (n = 5 at each time point). Data are respresented as means ± SD. The insets show organ-specifc imaging of ICR mice at 6 h after injection (Li, liver; S, spleen; Lu, lung; K, kidney).[171]

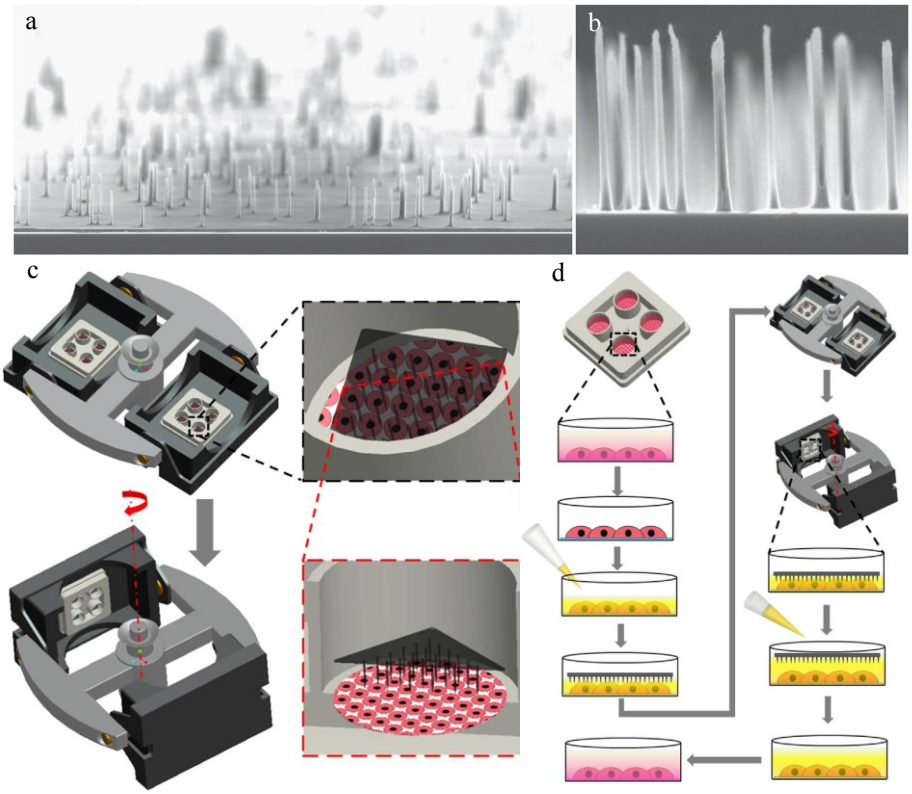

Fig. 15 (a) and (b) Characterization of diamond nanoneedle array. (a) Overall view (scale bar, 10 mm) and (b) detailed view (scale bar, 2 mm) of a nanoneedle array by scanning electron microscopy. (c) and (d) Schematic of the nanoneedle array-based intracellular delivery system. (c) Illustration of the basic design and working principle. (d) The work flow of the delivery procedures using nanoneedle arrays. The interaction between nanoneedles and cells was precisely controlled by centrifugation-induced supergravity to achieve reliable and efficient cytosolic delivery. Briefly, the culture medium was first removed, and replaced with basal medium containing materials to be delivered (fluorescent dye, dextran, antibody, nanoparticle, DNA, and so on). The solution volume was just enough to cover all the cells and to prevent cells from drying. A nanoneedle array was then placed onto the solution with nanoneedles facing towards cells, leaving a thin layer of solution between the nanoneedles and the cells. The whole setup was placed in a centrifuge and spun at various speeds. After centrifugation, extra basal medium (containing cargo materials at desired concentrations) was immediately added to the culture well to lift off the nanoneedle patch. After 5–30 min incubation at 37 °C, fresh culture medium was used to wash off extra materials and to culture the cells for further analysis. The nanoneedle patch was then cleaned with piranha solution for reuse.[23]

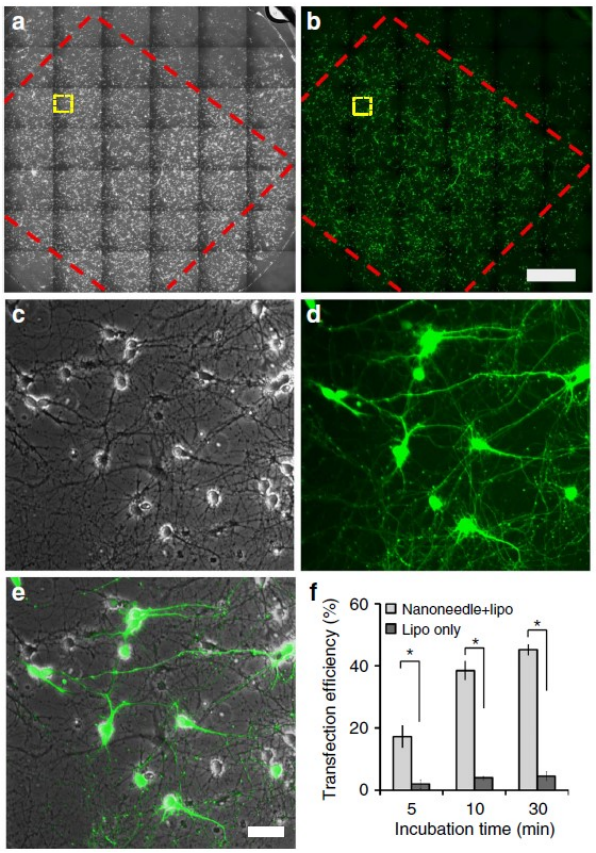

Fig. 16 Efficient cytosolic delivery of plasmid DNAs in neurons. (a) Stitched phase-contrast image of a neuron culture (6–7 DIV) treated by a nanoneedle patch. (b) Stitched fluorescent images of neurons transfected with GFP. In a,b, red squares indicate the area covered by the nanoneedle patch, scale bar, 1.6 mm. (c) Enlarged view of the yellow line boxed regions in a. (d) Enlarged view of the yellow line boxed regions in b. (e) Merged image of neuron cells combining phase-contrast and GFP channels; scale bar, 50 mm. (f) Comparison of the transfection efficiency between nanoneedle-based technique and traditional lipofection method at different incubation times, error bars indicate s.e.m. from three independent experiments. $^{*}p < 0.01$, determined by analysis of variance.[23]

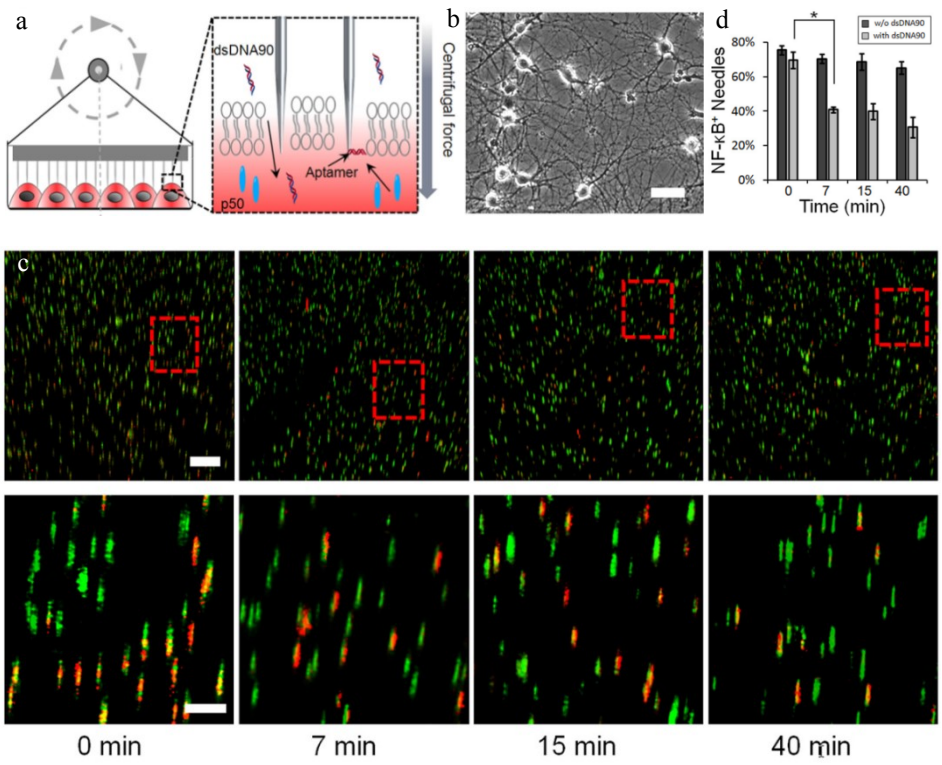

Fig. 17 Diamond-nanoneedle-assisted intracellular "molecular fishing". (a) Schematic of the centrifugation controlled intracellular insertion and probing process. (b-d) Interrogation of STING activated innate immune response in primary hippocampal neurons. (b) Phase-contrast image of cultured primary hippocampal neurons (9 days *in vitro*). Scale bar, 50 μm. (c) Combined fluorescence images showing colocalization of NF-κB speckles (red) with diamond-nanoneedles (green) at 0, 7, 15, and 40 min after intracellular delivery of dsDNA90. Scale bar, 20 μm. Enlarged views of the boxed region in the top row are shown in the bottom row. Scale bar, 5 μm. (d) Quantitative analysis of NF-κB positive nanoneedles with or without the STING activator (dsDNA90) in neuron cells at different experimental time points. Error bars indicate s.e.m. from three independent experiments. $^{*}P<0.001$ by ANOVA analysis.[213]

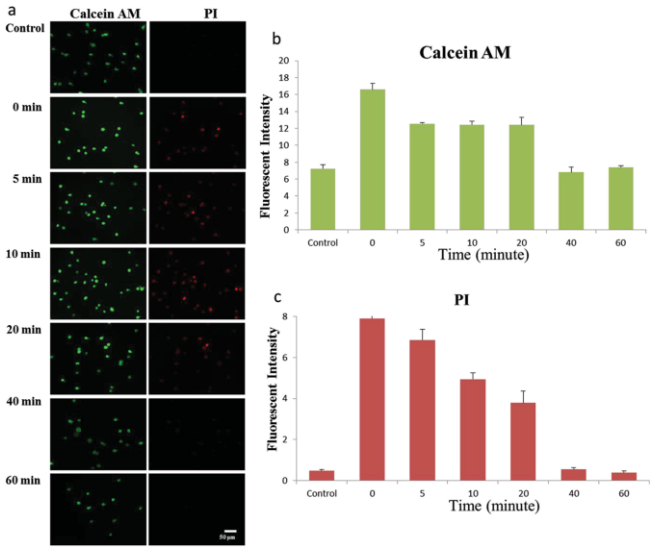

Fig. 18 Cytosolic delivery of calcein-AM and PI in A549 cells. a) Calcein-AM (left) and PI (right) fluorescent images of living A549 cells when the chemicals were added at different time points after the cells being treated with nanoneedles. b) Quantification of calcein-AM fluorescent intensity of different groups. c) Quantification of PI fluorescent intensity at different time points. Untreated A549 cells were set as a control group.[20]

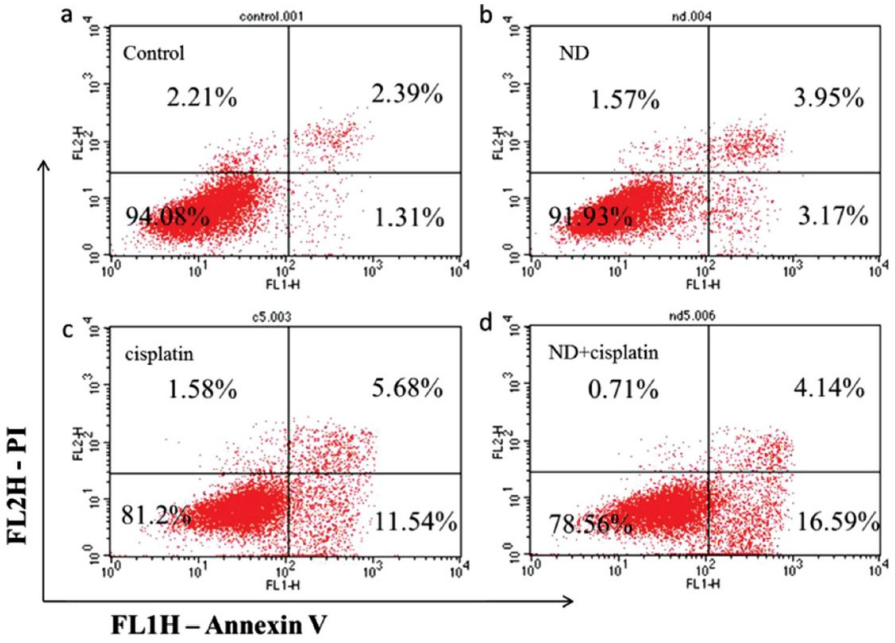

Fig. 19 Flow cytometry analysis of apoptosis and necrosis of A549 cells. a) Untreated cells; b) Cells treated with a diamond nanoneedle array (ND) alone; c) Cells incubated with 5 μg mL^{-1} of cisplatin for 24 h. d) Cisplatin was added to a cell suspension with a concentration of 5 μg mL^{-1} and the suspension was applied to a diamond nanoneedle array for treatment for 5 min. Subsequently, the cell suspension was collected and cultured in a 96-well plate for 24 h. The analysis was conducted after 24 h incubation. For all groups, A549 cells were stained and analysed by 488 nm excitation with 530/30 nm and 575/24 nm bandpass filters and collected by means of a standard 100 μL min^{-1} collection rate. Early apoptotic cells are shown in the lower right quadrant, and necrotic cells are shown in the upper left quadrant.[20]